

The oldest stars with low neutron-capture element abundances and origins in ancient dwarf galaxies

Hillary Diane Andales,^{1*} Ananda Santos Figueiredo,¹ Casey Gordon Fienberg,¹

Mohammad K. Mardini,^{2,3,4,1} Anna Frebel^{1,4}

¹*Department of Physics and Kavli Institute for Astrophysics and Space Research, Massachusetts Institute of Technology, Cambridge, MA 02139, USA*

²*Department of Physics, Zarqa University, Zarqa 13110, Jordan*

³*Jordanian Astronomical Virtual Observatory, Zarqa University, Zarqa 13110, Jordan*

⁴*Joint Institute for Nuclear Astrophysics – Center for the Evolution of the Elements (JINA-CEE), East Lansing, MI 48824, USA*

Accepted XXX. Received YYY; in original form ZZZ

ABSTRACT

We present a detailed chemical abundance and kinematic analysis of six extremely metal-poor ($-4.2 \leq [\text{Fe}/\text{H}] \leq -2.9$) halo stars with very low neutron-capture abundances ($[\text{Sr}/\text{H}]$ and $[\text{Ba}/\text{H}]$) based on high-resolution Magellan/MIKE spectra. Three of our stars have $[\text{Sr}/\text{Ba}]$ and $[\text{Sr}/\text{H}]$ ratios that resemble those of metal-poor stars in ultra-faint dwarf galaxies (UFDs). Since early UFDs may be the building blocks of the Milky Way, extremely metal-poor halo stars with low, UFD-like Sr and Ba abundances may thus be ancient stars from the earliest small galactic systems that were accreted by the proto-Milky Way. We label these objects as Small Accreted Stellar System (SASS) stars, and we find an additional 61 similar ones in the literature. A kinematic analysis of our sample and literature stars reveals them to be fast-moving halo objects, all with retrograde motion, indicating an accretion origin. Because SASS stars are much brighter than typical UFD stars, identifying them offers promising ways towards detailed studies of early star formation environments. From the chemical abundances of SASS stars, it appears that the earliest accreted systems were likely enriched by a few supernovae whose light element yields varied from system to system. Neutron-capture elements were sparsely produced and/or diluted, with r -process nucleosynthesis playing a role. These insights offer a glimpse into the early formation of the Galaxy. Using neutron-capture elements as a distinguishing criterion for early formation, we have access to a unique metal-poor population that consists of the oldest stars in the universe.

Key words: stars: abundances – stars: Population II – Galaxy: halo – nuclear reactions, nucleosynthesis, abundances – galaxies: dwarfs

1 INTRODUCTION

The Milky Way’s ultra-faint dwarf satellite galaxies (UFDs) continue to offer a vital window into the early universe. Besides providing insight on a broad range of astrophysical questions such as the formation of galaxies and structure (e.g., [Frebel & Bromm 2012](#); [Wheeler et al. 2015](#); [Kallivayalil et al. 2018](#); [Applebaum et al. 2021](#)) and the small-scale properties of dark matter (e.g., [Simon & Geha 2007](#); [Calabrese & Spergel 2016](#); [Brandt 2016](#); [Safarzadeh & Spergel 2020](#); [Orkney et al. 2022](#)), UFDs are uniquely important laboratories for studying the early universe. In particular, they provide a glimpse into early star formation environments, early chemical enrichment events, and the early assembly of the Milky Way (e.g., [Kirby et al. 2008](#); [Simon et al. 2010](#); [Roederer et al. 2018](#); [Lee et al. 2019](#); [Brauer et al. 2022](#)).

Formed 12 to 13 billion years ago at around $z \sim 10$ ([Brown et al. 2012, 2014](#); [Simon et al. 2023](#)), UFDs are ancient and thus extremely metal-poor ([Frebel et al. 2010a,b](#); [Ji et al. 2016c](#); [Chiti et al. 2018, 2021, 2023](#)). In fact, the majority of UFD stars have metallicities

between $[\text{Fe}/\text{H}] = -2$ and $[\text{Fe}/\text{H}] = -3$, with some stars reaching levels as low as $[\text{Fe}/\text{H}] = -4$ ([Simon 2019](#)). Most of their stars formed before reionization ($z \sim 6$) after which their star formation was quenched ([Weisz et al. 2014](#); [Brown et al. 2014](#)). Since the epoch of reionization, UFDs have been gas-poor, quiescent, and largely chemically unaltered ([Koch et al. 2009](#)). As a result, their long-lived metal-poor stars now carry clean signatures of the earliest chemical enrichment events in the universe, as well as hints about early star formation environments.

However, further progress in exploring the early universe using UFDs is severely hampered by the simple fact that UFDs are too distant. Because these tiny galaxies lie dozens or hundreds of kiloparsecs away, studying their chemical makeup with high-resolution spectroscopy is notoriously challenging. In principle, faint stars with visual magnitudes of $V \sim 19$ are still observable but such observations would be near the technical limits of current telescopes. Thus only a handful of UFD stars — the brightest cool red giants — are available for high-resolution spectroscopy. Much fainter stars are much more difficult to observe, even with medium-resolution spectroscopy. As a result, the current chemical abundance datasets on UFDs are still too sparse and inadequate; only a few dozen UFD stars have de-

* E-mail: handales@mit.edu

tailed chemical abundances (Suda et al. 2017; Abohalima & Frebel 2018). To get around this, one common solution is to combine stars from various UFDs and treat that combination as one "population" (e.g., Vargas et al. 2013). Yet, even with this workaround, most of the chemical abundance data still have large uncertainties.

Unraveling the histories of UFDs requires more detailed probing, much more than the current chemical abundance datasets can allow. We thus suggest an alternative path forward: searching in the Galactic halo for erstwhile member stars of small satellites that were accreted by the Milky Way billions of years ago. After all, the Milky Way assembled hierarchically, and presumably many small "building block" systems — including possible analogs of the surviving UFDs — contributed to its early formation (e.g., Wetzel et al. 2016; Griffen et al. 2016). Stars from these small accreted systems could therefore be suitable analogs of the stars in surviving UFDs. Using these analog stars is obviously advantageous for detailed chemical study since halo stars are more numerous and more accessible for high-resolution spectroscopy.

To isolate these analogs from the broader collection of halo stars, we look for stars with similar chemical properties as those in extant UFDs. First, they must be metal-poor since UFD stars are typically Very Metal-Poor (VMP; $[\text{Fe}/\text{H}] < -2$) or Extremely Metal-Poor (EMP; $[\text{Fe}/\text{H}] < -3$). Second, unlike VMP and EMP stars in the halo, we would expect most UFD stars not to show significant carbon enhancements (where carbon enhancement is defined as $[\text{C}/\text{Fe}] > 0.7$). This discrepancy is well-established and works in our favor here (Frebel et al. 2010b). Third, they must have extraordinarily low abundances of neutron-capture elements (e.g., Sr and Ba). Finally, they must have retrograde motion consistent with an accretion origin. Previous works have used some combination of these criteria to associate halo stars with their possible origins in now-destroyed UFD-like satellites, effectively finding some of our possible analog stars (Hansen et al. 2016a; Lee et al. 2017; Yoon et al. 2018; Yuan et al. 2020). Intriguingly, Sestito et al. (2024) even found a VMP star in the inner Galaxy with putative origins in an accreted UFD.

Low neutron-capture abundance is the hallmark characteristic of UFD stars that sets them apart from the general halo trend (Ji et al. 2019). Many chemical abundance studies have consistently found low $[\text{Sr}/\text{Fe}]$ and $[\text{Ba}/\text{Fe}]$ across all UFD stars, with their neutron capture abundances being as much as ~ 1 dex lower than a halo star of the same metallicity (Frebel et al. 2010a,b, 2014; Frebel 2018; Ji et al. 2020). When normalizing the Sr and Ba abundances to H instead of Fe to determine the overall neutron-capture enrichment level (i.e., by examining $[\text{Sr},\text{Ba}/\text{H}]$ instead of $[\text{Sr},\text{Ba}/\text{Fe}]$), Frebel et al. (2014) found a cleaner cut between halo stars and UFD stars, such that the latter are predominantly found with abundance levels at $[\text{Sr}/\text{H}] \lesssim -4$ and $[\text{Ba}/\text{H}] \lesssim -3.5$. Two exceptions to this rule are Reticulum II and Tucana III which show an overabundance of neutron-capture elements due to a rare *r*-process enrichment event (Ji et al. 2016b; Roederer et al. 2016; Marshall et al. 2019). Even then, two of the stars in Reticulum II still display the characteristic low neutron-capture abundances. Indeed, this chemical criterion has been crucial in evaluating the membership of candidate UFD stars (e.g., Chiti et al. 2023).

In this paper, we thus set out to identify metal-poor halo stars that possibly originated from small satellite galaxies, and were presumably accreted by the Milky Way long ago. We developed abundance criteria in line with chemical signatures observed among UFD stars. We then apply these criteria to our program stars and to other stars with chemical abundances from the literature. Our goal was to assemble a set of stars that could be used as local probes of the population of small satellites that assembled the Galactic halo.

We later label these probes "Small Accreted Stellar System stars" or "SASS stars." These long-lived SASS stars offer an opportunity to study, in detail, the nucleosynthesis histories of early small galaxies, their environments, and early star formation. This complements the many ongoing studies of current UFDs. Detailed comparisons of the chemical abundances of our newly identified SASS stars with those in surviving UFDs would allow for further establishing to what extent the surviving UFDs are related to the first galaxies, or at least, the earliest assembled systems (Frebel et al. 2014).

In Section 2, we describe the initial target selection of our candidates and the spectroscopic observations. Sections 3 and 4 detail the chemical abundance analysis and our results. Section 5 presents the kinematic analysis of our program stars. In Section 6, we discuss our refined selection criteria for identifying SASS stars, taking into account a detailed kinematic analysis of our sample stars and considering the context of the Galactic halo's assembly. In the same section, we present possible enrichment scenarios and clues about the environments in early dwarf galaxies. We also offer future directions for identifying more SASS stars. Finally in Section 7, we summarize our work.

2 OBSERVATIONS AND MEASUREMENTS

2.1 Initial target selection and existing observations

All of our program stars were initially selected for high-resolution follow-up spectroscopy based on their brightness and low $[\text{Fe}/\text{H}]$ as determined from the medium-resolution spectra obtained during the Hamburg/ESO survey (Wisotzki et al. 1996; Frebel et al. 2006). For this subset of stars, high-resolution spectroscopy was then obtained over several years (described further below) with the goal of carrying out a detailed chemical abundance analysis. From this sample of high-resolution spectra, we visually selected stars that showed very weak or no Ba line at 4554 Å. This preliminary selection was to establish an exploratory sample for the current study on halo stars with possible origins in long-accreted small satellite systems.

Since data collection occurred back in 2013 and 2014, the majority of our program stars have already been observed by other groups for a variety of purposes. Given our generally high(er) data quality, we nevertheless decided to (re-)analyze these stars to obtain our independent measurements.

HE 0104–5300 was part of the large Barklem et al. (2005) and Jacobson et al. (2015) samples that provided detailed chemical abundances. The spectrum used in the present study is the same spectrum analyzed by Jacobson et al. (2015), allowing for a detailed abundance comparison between their work and this work.

HE 1310–0536 was also observed by Hansen et al. (2014) and noted for its low Ba and Sr abundances. Their data had a signal-to-noise ratio (S/N) of ~ 40 at 4300 Å (65 at 6700 Å) whereas our spectrum has a S/N of 40 at 4000 Å and ~ 80 at 4500 Å, around where the strongest Sr and Ba absorption lines are located. Hansen et al. (2014) found $[\text{Sr}/\text{Fe}] = -1.08$ and $[\text{Ba}/\text{Fe}] = -0.50$. As we will show in Section 4, we find somewhat lower values likely due to our increased S/N .

Two of our carbon-rich stars, HE 2319–5228 and HE 2155–2043, were analyzed by Hansen et al. (2016b) and were both found to have extremely low abundances of heavy neutron-capture elements. Our spectra are of better quality than those presented in Hansen et al. (2016b). Their spectrum of HE 2319–5228 had a S/N of 20 at 4000 Å compared to our ~ 40 . Their spectrum of HE 2155–2043 was reported at 40, while we have ~ 50 .

Table 1. Observing details and heliocentric velocities

Star	RA [J2000]	Dec [J2000]	UT Dates	Slit	t_{exp} [s]	g [mag]	S/N [4000 Å]	S/N [4500 Å]	V_{helio} [km s ⁻¹]	$V_{\text{helio, Gaia}}$ [km s ⁻¹]
HE 0104–5300	01:06:51.9	–52:44:10.5	Jan 6, 2013	1''0 × 5''0	1800	14.1	63	111	188.3	186.6
HE 1310–0536	13:13:31.1	–05:52:12.5	Mar 11, 2014	0''7 × 5''0	3600	14.1	40	81	110.9	108.3
HE 2155–2043	21:58:42.2	–20:29:15.7	May 31, 2013	0''7 × 5''0	4339	13.0	49	83	–94.8	–90.8
HE 2303–5756	23:06:55.1	–57:40:33.5	Jun 22, 2014	0''7 × 5''0	1200	13.1	80	122	–85.4	–92.8
HE 2319–5228	23:21:58.1	–52:11:43.2	Jun 23, 2014	0''7 × 5''0	900	13.0	37	45	292.8	284.2
HE 2340–6036	23:43:41.1	–60:19:22.4	Sep 25, 2014	0''7 × 5''0	1200	12.5	45	74	212.4	212.1

For HE 2319–5228, they report upper limits of $[\text{Ba}/\text{Fe}] < -3$ and $[\text{Sr}/\text{Fe}] < -3$. For HE 2155–2043, they report $[\text{Sr}/\text{Fe}] = 0.2$, and no value for $[\text{Ba}/\text{Fe}]$.

HE 2155–2043 was also analyzed by [Purandardas & Goswami \(2021\)](#), but no S/N was reported of the spectra taken from the Subaru Telescope archive. They reported $[\text{Sr}/\text{Fe}] = -0.13$ and $[\text{Ba}/\text{Fe}] = -1.51$. Our spectrum has a relatively high S/N of ~ 50 at 4000 Å and ~ 80 at 4500 Å. In Section 4, we will compare abundances in more detail.

HE 2340–6036 was included in the r -process Alliance’s [Holmbeck et al. \(2020\)](#) data release. A S/N of 22 was reported at 4129 Å of their snapshot spectrum, compared to our S/N of 45 at 4000 Å and 74 at 4500 Å. They reported weak Sr and Ba lines, finding $[\text{Sr}/\text{Fe}]$ of -1.89 and $[\text{Ba}/\text{Fe}]$ of -1.34 . We will report somewhat higher abundances in Section 4.

Finally, we present the first detailed chemical abundance analysis of HE 2303–5756.

2.2 High-resolution spectroscopy

All of our stars were observed at Las Campanas Observatory in January and May of 2013, as well as March, June, and September of 2014 using the Magellan Inamori Kyocera Echelle (MIKE) instrument ([Bernstein et al. 2003](#)) on the Magellan-Clay telescope. Data for all program stars except HE 0104–5300 was taken with a slit size of $0''.7 \times 5''.0$, resulting in a resolving power of $\sim 28,000$ in the red wavelength and $\sim 35,000$ in the blue. Data for HE 0104–5300 was obtained with a $1''.0 \times 5''.0$ slit, yielding a resolving power of $\sim 22,000$ and $\sim 28,000$ for the red and blue spectra, respectively. Exposure times ranged from 900 to roughly 4500 seconds.

We used the CarPy MIKE pipeline (the version available at the time) to reduce all spectra ([Kelson 2003](#)). Using the SMH custom analysis software ([Casey 2014](#)), we normalized and stitched all blue and red echelle orders together before Doppler correcting the spectra by cross-correlation. We employed HD122563 as a template using the Ca triplet lines around 8500 Å. Heliocentric velocities were determined using standard Python packages. Observational details and radial velocity measurements are listed in Table 1. Figure 1 shows three selected spectral regions of the final spectra of all our stars: around the Sr line at 4077 Å, the CH G-band around 4300 Å, and the Ba line at 4554 Å.

We also list *Gaia* radial velocities in Table 1 for comparison with our derived values. The measurements generally agree within a few km s⁻¹. The largest differences are found for HE 2319–5228 and HE 2303–5756 for which the radial velocities differ by nearly 10 km s⁻¹, suggesting that these stars are part of binary systems. Searching for additional radial velocity measurements in the SIMBAD database reveals further support for their binarity. We note that neither of the two stars appears to be a double-lined spectroscopic binary so our spectra are not affected by any light from a presumably faint companion.

HE 2319–5228 is very carbon-enhanced which could be due to a mass transfer event from its previously more massive companion. Since it is not s -process-enriched, as is common for carbon-rich stars in binary systems, it may have had a relatively massive erstwhile AGB companion. An alternative enrichment scenario that could explain the observed abundances is a massive, rapidly rotating “spinstar” that produced large amounts of carbon and then enriched the natal gas cloud of HE 2319–5228 ([Chiappini et al. 2006](#); [Cescutti et al. 2013](#); [Meynet et al. 2006](#); [Hirschi 2006](#)). If such spinstars were present among later generations of stars (not just among Pop III stars), then HE 2319–5228 may have had a spinstar companion that transferred carbon-rich mass into it.

3 CHEMICAL ABUNDANCE ANALYSIS

3.1 Line measurements

To determine the chemical abundances of our stars, we utilize a line list from [linemake¹](#) ([Placco et al. 2021](#)) that contains absorption lines of various elements. We measure the strength of clean spectral lines by fitting Gaussian profiles to each absorption feature, after which we obtain their equivalent widths (EWs). Only lines between 3500 Å and 7000 Å were used. Below 4000 Å the S/N becomes lower, making good line measurements challenging. To ensure that EWs are on the linear part of the curve of growth, only lines with reduced EWs less than -4.5 were used. Some exceptions were made for elements with few lines, such as Na, but line abundances were always individually checked for consistency.

EW measurements are not useful for spectral features that are blended, lines with hyperfine structure, and molecular bands (e.g., CH). In those cases, we used the spectrum synthesis approach to obtain the line abundance where we fit a synthetic spectrum with a known abundance to the observed spectrum. Spectrum synthesis was performed for features of C, Si, Al, Sc, Mn, Co, Sr, Ba, and Eu. We also determined 3σ upper limits on the abundances of any pertinent, undetected lines. Table 2 lists all our measured EWs (where available) and their corresponding abundances.

3.2 Stellar Parameters

We determine photometric stellar parameters using parallaxes and proper motion data from *Gaia* (where available) and our line measurements of Fe I and Fe II lines. First, we determine the effective temperature (T_{eff}) using the $V - K$ color-temperature-metallicity formula presented in [Casagrande et al. \(2010\)](#). Using the United States Naval Observatory UCAC4 Catalog² ([Zacharias et al. 2013](#)), we utilize J and K magnitudes from 2MASS (Two Micron All-Sky Survey) and

¹ Available at <https://github.com/vmplacco/linemake>

² Accessible via [NASA/IPAC Infrared Science Archive](#)

Table 2. Equivalent widths measurements and line abundances of our program stars

Species	λ [Å]	χ [eV]	$\log gf$ [dex]	HE 0104–5756		HE 1310–0536		HE 2155–2043		HE 2303–5756		HE 2319–5228		HE 2340–6036	
				EW [mÅ]	$\log \epsilon(X)$ [dex]	EW [mÅ]	$\log \epsilon(X)$ [dex]	EW [mÅ]	$\log \epsilon(X)$ [dex]	EW [mÅ]	$\log \epsilon(X)$ [dex]	EW [mÅ]	$\log \epsilon(X)$ [dex]	EW [mÅ]	$\log \epsilon(X)$ [dex]
CH	4314.00	4.80	...	6.29	...	6.00	...	6.30	...	6.27	...	4.26
CH	4323.00	4.74	...	6.21	...	5.99	...	5.93	...	6.26	...	4.28
Na I	5682.63	2.10	-0.71	28.1	4.78
Na I	5688.20	2.10	-0.41	33.2	4.58
Na I	5889.95	0.00	+0.11	113.0	2.84	70.4	2.20	139.6	3.52	45.2	3.07	265.8	4.51	143.4	3.19
Na I	5895.92	0.00	-0.19	107.6	3.04	48.4	2.14	106.4	3.22	22.7	2.93	242.4	4.69	127.1	3.23
Mg I	4057.51	4.35	-0.90	11.2	4.56	14.0	4.61
Mg I	4167.27	4.35	-0.74	18.7	4.65	6.9	4.88	22.2	4.68
Mg I	4702.99	4.33	-0.44	24.4	4.44	10.4	4.00	35.1	4.76	10.5	4.74	58.9	5.03	36.5	4.60
Mg I	5172.68	2.71	-0.36	141.1	4.38	88.1	3.60	147.2	4.70	89.5	4.81	176.0	4.83	160.4	4.45
Mg I	5183.60	2.72	-0.17	160.1	4.46	105.4	3.76	163.0	4.75	104.0	4.90	187.4	4.75	177.2	4.45
Al I	3944.00	0.00	-0.64	...	2.60	...	2.08	2.76	2.34
Al I	3961.52	0.01	-0.34	...	2.13	...	1.31	2.71	...	2.82	...	2.30
Si I	3905.52	1.91	-1.09	...	4.54	4.67	...	4.92	...	4.61
Si I	4102.94	1.91	-3.14	4.23	...	4.98

This table is available in its entirety in the online journal.

Table 3. Photometry and astrometry for our program stars

Star	<i>Gaia</i> Source ID	J	K	V	A_V	$E(B - V)$	parallax (mas)
HE 0104–5300	4927175937828177280	11.91 ± 0.03	11.29 ± 0.02	13.63 ± 0.03	0.0326	0.0108 ± 0.0004	0.0999 ± 0.0112
HE 1310–0536	3635533208672382592	12.53 ± 0.02	12.05 ± 0.02	14.38 ± 0.02	0.1149	0.0368 ± 0.0016	0.0118 ± 0.0232
HE 2155–2043	6823219517280229120	11.57 ± 0.02	11.02 ± 0.02	13.23 ± 0.01	0.0799	0.0257 ± 0.0006	0.1240 ± 0.0301
HE 2303–5756	6493230587155263360	12.23 ± 0.02	11.91 ± 0.02	13.24 ± 0.02	0.0455	0.0147 ± 0.0005	0.9229 ± 0.0166
HE 2319–5228	6501398446721935744	11.55 ± 0.02	10.96 ± 0.02	13.25 ± 0.02	0.0277	0.0087 ± 0.0005	0.1616 ± 0.0158
HE 2340–6036	6488378098744387968	11.05 ± 0.02	10.40 ± 0.02	12.83 ± 0.01	0.0363	0.0119 ± 0.0002	0.1666 ± 0.0126

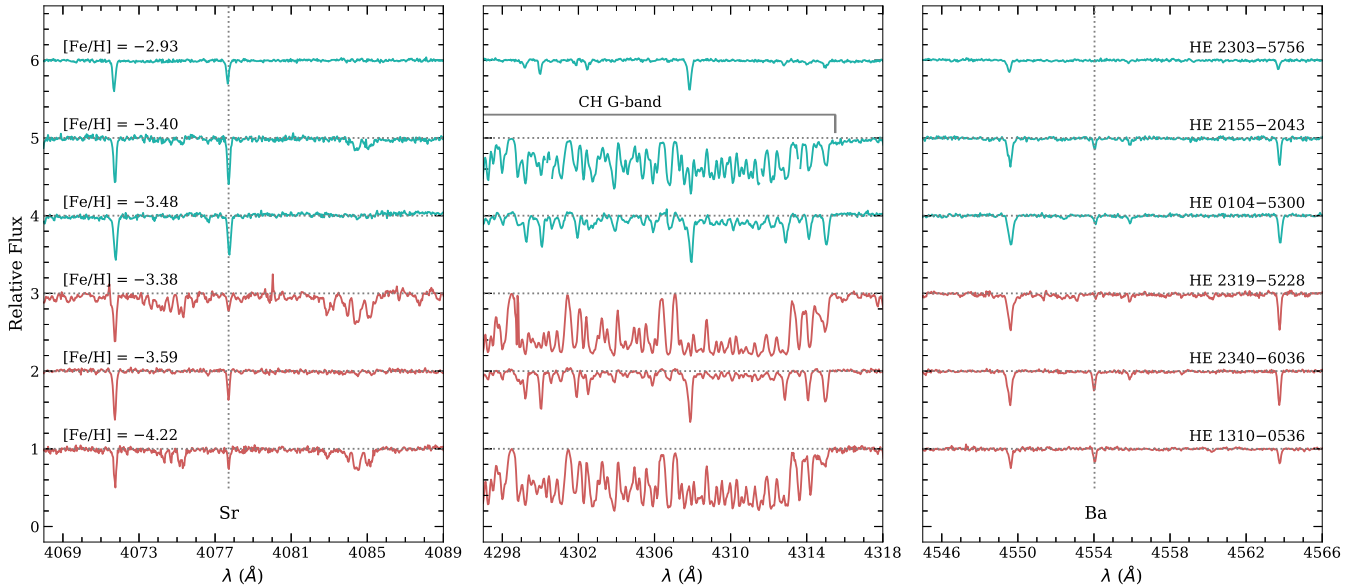


Figure 1. Spectra of our program stars around the Sr line at 4077 Å, the carbon G-band around 4300 Å, and the Ba line at 4554 Å. The top three spectra (teal) are halo stars from our sample (HE 2303–5756, HE 2155–2043, HE 0104–5300), whereas the bottom three spectra (red) depict stars with putative origins in long-accreted small satellite systems (HE 2319–5228, HE 2340–6036, HE 1310–0536). Spectra were shifted vertically to aid visual representation. Note that HE 2303–5756 (teal) and HE 2319–5228 (red) appear to be in binary systems.

V magnitudes from APASS (AAVSO Photometric All-Sky Survey). To correct for dust reddening, we use the extinction (A_V) and reddening $E(B - V)$ values from the dust maps by [Schlafly & Finkbeiner \(2011\)](#). Values are listed in Table 3. As necessary, we iterate on the temperature determination with our simultaneous metallicity determination.

We calculate the surface gravity ($\log g$) by minimizing the trend between Fe I and Fe II lines. The values are listed in Table 4. We then test the robustness of our results by re-deriving $\log g$ using a different method, specifically the one used in [Mardini et al. \(2019\)](#). This method uses dereddened g magnitudes from APASS (compiled on the UCAC4 catalog), parallaxes π from *Gaia* DR3

([Gaia Collaboration et al. 2022](#)), and fundamental equations with respect to the Sun. The surface gravity values derived with both methods agree within 1σ .

Generally, our stellar parameters agree well with those obtained by other studies (e.g., [Jacobson et al. 2015](#)). For one star, HE 1310–0536, our T_{eff} of ~ 4700 K is lower than that derived by [Hansen et al. \(2014\)](#) ($T_{\text{eff}} = 5000$ K). However, a visual comparison of this star’s H β absorption line profile with those of stars with known temperatures — namely CS22892-52 ($T_{\text{eff}} = 4620$ K) and HE 1523–0901 ($T_{\text{eff}} = 4370$ K) — well supports $T_{\text{eff}} < 5000$ K.

For our abundance calculations, we adopt 1D plane-parallel model atmospheres with α -enhancement (generated using the values listed

Table 4. Stellar parameters

Star	T_{eff} [K]	$\log g$ [cgs]	[Fe/H] [dex]	v_{mic} [km s ⁻¹]
HE 0104–5300	4791	1.82	-3.48 ± 0.15	1.95
HE 1310–0536	4668	0.57	-4.22 ± 0.14	1.84
HE 2155–2043	4994	1.82	-3.40 ± 0.17	2.02
HE 2303–5756	6349	3.60	-2.93 ± 0.10	1.53
HE 2319–5228	4836	2.09	-3.38 ± 0.12	1.70
HE 2340–6036	4689	1.93	-3.59 ± 0.17	1.91

in Table 4) from [Castelli & Kurucz \(2004\)](#). We used the latest version of the MOOG radiative transfer code ([Snedden 1973](#); [Sobeck et al. 2011](#)) and assumed local thermodynamic equilibrium (LTE). This MOOG version includes scattering effects. We then obtain the Fe abundance for each star using their respective effective temperatures and surface gravities, as determined above and including any iterations.

In the process of determining the Fe abundances, we also derived the microturbulence (v_{mic}) for each star by forcing no trend between Fe I line abundance and reduced equivalent widths. All our abundance ratios ($[X/\text{Fe}]$ and $[X/\text{H}]$) are calculated relative to the solar abundances determined by [Asplund et al. \(2009\)](#). Our final and adopted stellar parameters are given in Table 4.

4 CHEMICAL ABUNDANCE RESULTS

In Table 5, we present the results of our detailed chemical abundance analysis of 17 elements in our sample stars. In Figure 2, we show our sample stars in comparison with a general set of metal-poor halo stars ([Cayrel et al. 2004](#); [Barklem et al. 2005](#); [Yong et al. 2013](#)) and with metal-poor stars in various UFDs³ ([Koch et al. 2008](#); [Simon et al. 2010](#); [François et al. 2016](#); [Frebel 2010](#); [Norris et al. 2010](#); [Ji et al. 2016b](#); [Koch et al. 2013](#); [Gilmore et al. 2013](#); [Ishigaki et al. 2014](#); [Frebel et al. 2014](#); [Ji et al. 2016a](#); [Roederer et al. 2016](#); [Frebel et al. 2016](#); [Kirby et al. 2017](#); [Spite et al. 2018](#); [Chiti et al. 2018](#); [Nagasawa et al. 2018](#); [Ji et al. 2019](#); [Marshall et al. 2019](#); [Ji et al. 2020](#); [Hansen et al. 2020](#); [Waller et al. 2022](#); [Chiti et al. 2022](#)). In the following, we discuss notable results and abundance trends. Further discussion of the origins of our stars and their possible relations to early, small dwarf galaxies will come in Section 6.

As mentioned in Section 3.2, we derived $\log g$ using two methods, i.e., spectroscopically versus using photometry and parallax. To err on the side of caution, we tested whether changes in stellar parameters affected the chemical abundances. We found that the abundances were not significantly altered. Since our abundance measurements are robust to changes in $\log g$, from this point onward we will only report abundances obtained using the spectroscopically-derived $\log g$.

4.1 Carbon abundances

The most metal-poor halo stars with $[\text{Fe}/\text{H}] < -2.5$ have long been known to have predominantly very large carbon abundances (e.g., [Frebel et al. 2005](#); [Placco et al. 2014b](#); [Hansen et al. 2016a](#); [Lee et al. 2017](#); [Yoon et al. 2018](#)). In general, carbon enhancement is defined as $[\text{C}/\text{Fe}] > 0.7$ ([Aoki et al. 2007](#)). As stars ascend the giant branch, carbon abundances get depleted. We correct for this fact using models provided in [Placco et al. \(2014b\)](#). Our sample shows a

large variety of $[\text{C}/\text{Fe}]$, as measured from the carbon G-band head around 4313 Å and the feature at 4323 Å (see Figure 1). We used spectrum synthesis on each spectral feature to infer the star’s carbon abundance, after which we averaged the measurements on both features to obtain the star’s final carbon abundance.

Three of our program stars, HE 1310–0536, HE 2155–2043, and HE 2319–5228 can thus be classified as carbon-enhanced metal-poor (CEMP) stars. HE 1310–0536, with the lowest $[\text{Fe}/\text{H}]$ of -4.22 , strongly follows the halo trend having $[\text{C}/\text{Fe}] = 2.7$ (corrected). The other two stars have corrected abundances around $[\text{C}/\text{Fe}] \sim 1.2$ and also support the halo trend. In contrast, two of our sample stars have very low, subsolar carbon abundances (HE 2340–6036 and HE 0104–5300) at $[\text{Fe}/\text{H}] \sim -3.5$.

4.2 Light and iron-peak element abundance trends

In general, our stars’ chemical abundances agree well with the overall abundance trends of halo and dwarf galaxy stars. However, it is interesting to note that we do see a significant spread among our six stars. We recall in this context that these stars were selected only visually for their having a weak or no Ba line in their spectrum. This selection alone might imply a certain level of heterogeneity among light and iron-peak elements as measured in our sample but it may not warrant it either. In Figure 2, it can be seen that for several elements (Al, Ca, Ti, Co, Ni), the stars denoted by squares (HE 1310–0536, HE 2340–6036, HE 2319–5228) differ somewhat from the stars denoted by triangles (HE 0104–5300, HE 2155–2043, HE 2303–5756). We chose to group these stars by shape according to their behaviour in the $[\text{Sr}/\text{Ba}]$ versus $[\text{Ba}/\text{Fe}]$ plot (see Figure 3 and Section 4.3). Stars denoted by squares behave like UFD stars in Figure 3 while those denoted by triangles agree with typical halo star $[\text{Sr}/\text{Ba}]$ behavior.

Generally, the stars denoted by triangles reasonably follow the overall halo trends in their light element abundances. Meanwhile, the stars denoted by squares tend to deviate from them. For Zn, we only have two measurements, so no strong conclusions can be derived. However, the upper limit of HE 1310–0536, our most metal-poor star, is significantly lower than the halo trend. We thus add Zn to the list of elements for which the two star groups show different behavior.

4.3 Heavy element abundance trends

Sr was detected in all six of our sample stars. All have $[\text{Sr}/\text{H}] < -3$, and three have a remarkably low abundance of $[\text{Sr}/\text{H}] \lesssim -5$. Ba abundances were determined for all stars except HE 2303–5756, for which only an upper limit of $[\text{Ba}/\text{H}] < -3.93$ was found. The other five stars all had $[\text{Ba}/\text{H}] < -4.0$, with three having $[\text{Ba}/\text{H}] < -5.0$. For $[\text{Sr}/\text{H}]$ and $[\text{Ba}/\text{H}]$, all stars follow the general halo trend.

To classify our stars and learn about the origin(s) of their neutron-capture elements, we plot $[\text{Sr}/\text{Ba}]$ versus $[\text{Ba}/\text{Fe}]$ in Figure 3. This offers a way to empirically learn about the nucleosynthesis processes that may have produced these elements, as it remains unclear what underlying nucleosynthesis processes cause the observed differences between typical halo stars and stars in UFDs. As has been shown in [Frebel et al. \(2014\)](#) and [Ji et al. \(2019\)](#), in this type of plot, the UFD stars are removed from the halo stars that form the main branch. Instead, they form their own branch at lower $[\text{Sr}/\text{Ba}]$ values. This clustering is immediately evident in Figure 3.

We find that three of our stars, HE 2303–5756, HE 2155–2043, and HE 0104–5300, are located along the main halo branch. Meanwhile, the three other stars, HE 2319–5228, HE 1310–0536, and HE 2340–6036, are squarely within the region occupied by the UFD

³ Compilation by AP Ji available on [GitHub](#)

Table 5. Chemical abundances of our program stars

Species	<i>N</i>	$\log \epsilon (X)$	stderr	[X/H]	[X/Fe]	Species	<i>N</i>	$\log \epsilon (X)$	stderr	[X/H]	[X/Fe]
HE 0104–5300						HE 1310–0536					
C (CH)	2	4.77	0.10	−3.66	−0.17	C (CH)	2	6.25	0.10	−2.18	2.04
C (CH) _{corr}	−0.11	C (CH) _{corr}	2.67
Na I	2	2.94	0.13	−3.30	0.18	Na I	2	2.17	0.05	−4.07	0.15
Mg I	5	4.50	0.05	−3.10	0.38	Mg I	6	3.84	0.06	−3.76	0.46
Al I	2	2.37	0.42	−4.08	−0.60	Al I	2	1.70	0.51	−4.75	−0.53
Si I	2	4.67	0.16	−2.84	0.64	Si I	1	3.68	0.15	−3.83	0.39
Ca I	14	3.22	0.05	−3.12	0.36	Ca I	6	2.78	0.05	−3.56	0.66
Sc II	6	−0.29	0.05	−3.44	0.05	Sc II	1	−1.19	0.15	−4.34	−0.12
Ti I	12	1.74	0.05	−3.21	0.27	Ti I	3	1.19	0.24	−3.76	0.47
Ti II	21	1.91	0.05	−3.04	0.45	Ti II	14	1.28	0.05	−3.67	0.55
Cr I	5	1.89	0.13	−3.75	−0.26	Cr I	1	1.07	0.15	−4.57	−0.35
Mn I	1	1.07	0.15	−4.36	−0.88	Mn I	1	0.36	0.15	−5.07	−0.85
Fe I	116	4.02	0.05	−3.48	0.00	Fe I	43	3.28	0.10	−4.22	0.00
Fe II	13	4.27	0.05	−3.23	0.25	Fe II	2	3.25	0.33	−4.25	−0.03
Co I	3	1.82	0.05	−3.17	0.31	Co I	2	0.86	0.05	−4.13	0.09
Ni I	6	2.92	0.12	−3.30	0.18	Ni I	6	1.95	0.07	−4.27	−0.05
Zn I	1	1.64	0.15	−2.92	0.56	Zn I	1	< 0.57	...	< −3.98	< 0.24
Sr II	2	−1.02	0.05	−3.89	−0.40	Sr II	1	−2.99	0.15	−5.86	−1.64
Ba II	2	−2.71	0.05	−4.89	−1.41	Ba II	2	−2.92	0.15	−5.10	−0.88
Eu II	1	< −2.62	...	< −3.14	< 0.34	Eu II	1	< −3.20	...	< −3.72	< 0.50
HE 2155–2043						HE 2303–5756					
C (CH)	2	6.00	0.10	−2.43	0.97	C (CH)	2	6.11	0.35	−2.32	0.61
C (CH) _{corr}	1.07	C (CH) _{corr}	0.61
Na I	2	3.37	0.21	−2.87	0.54	Na I	2	3.00	0.09	−3.24	−0.31
Mg I	8	4.72	0.05	−2.88	0.53	Mg I	7	4.82	0.05	−2.78	0.15
Al I	1	2.29	0.10	−4.16	−0.76	Al I	2	2.74	0.05	−3.71	−0.79
Si I	1	4.06	0.20	−3.45	−0.04	Si I	1	4.67	0.15	−2.84	0.09
Ca I	11	3.32	0.05	−3.02	0.38	Ca I	9	3.76	0.05	−2.58	0.34
Sc II	5	−0.22	0.05	−3.37	0.03	Sc II	4	0.29	0.05	−2.86	0.06
Ti I	8	1.93	0.08	−3.02	0.38	Ti I	3	2.62	0.05	−2.33	0.60
Ti II	17	1.70	0.05	−3.25	0.15	Ti II	14	2.23	0.05	−2.72	0.21
Cr I	3	1.93	0.05	−3.71	−0.30	Cr I	4	2.62	0.05	−3.02	−0.09
Mn I	1	1.29	0.20	−4.14	−0.73	Mn I	1	1.94	0.15	−3.49	−0.57
Fe I	110	4.10	0.05	−3.40	0.00	Fe I	67	4.57	0.05	−2.93	0.00
Fe II	10	4.18	0.05	−3.32	0.08	Fe II	5	4.53	0.05	−2.97	−0.04
Co I	7	2.05	0.05	−2.94	0.47	Co I	6	2.47	0.05	−2.52	0.41
Ni I	11	2.92	0.05	−3.30	0.10	Ni I	13	3.52	0.05	−2.70	0.23
Zn I	2	1.77	0.21	−2.79	0.61	Zn I	1	< 2.16	...	< −2.40	< 0.53
Sr II	2	−0.76	0.06	−3.63	−0.23	Sr II	2	−0.47	0.05	−3.34	−0.41
Ba II	1	−2.38	0.08	−4.56	−1.16	Ba II	1	< −1.75	...	< −3.93	< −1.00
Eu II	1	< −2.50	...	< −3.02	< 0.38	Eu II	1	< −1.42	...	< −1.94	< 0.99
HE 2319–5228						HE 2340–6036					
C (CH)	2	6.27	0.10	−2.16	1.21	C (CH)	2	4.27	0.15	−4.16	−0.56
C (CH) _{corr}	1.22	C (CH) _{corr}	−0.55
Na I	4	4.64	0.07	−1.60	1.78	Na I	2	3.21	0.05	−3.03	0.56
Mg I	3	4.87	0.10	−2.73	0.65	Mg I	5	4.56	0.05	−3.04	0.55
Al I	1	2.82	0.20	−3.63	−0.25	Al I	2	2.32	0.05	−4.13	−0.53
Si I	2	5.07	0.05	−2.44	0.94	Si I	2	4.79	0.23	−2.72	0.88
Ca I	17	3.96	0.05	−2.38	0.99	Ca I	13	3.40	0.05	−2.94	0.65
Sc II	6	0.06	0.05	−3.09	0.29	Sc II	6	−0.21	0.05	−3.36	0.24
Ti I	7	1.99	0.05	−2.96	0.42	Ti I	9	1.58	0.05	−3.37	0.22
Ti II	17	2.34	0.05	−2.61	0.77	Ti II	21	1.95	0.05	−3.00	0.59
Cr I	3	2.11	0.17	−3.53	−0.15	Cr I	4	1.54	0.08	−4.10	−0.50
Mn I	2	1.40	0.15	−4.03	−0.66	Mn I	1	0.70	0.15	−4.73	−1.14
Fe I	59	4.12	0.05	−3.38	0.00	Fe I	86	3.91	0.05	−3.59	0.00
Fe II	6	4.29	0.05	−3.21	0.16	Fe II	8	4.23	0.07	−3.27	0.32
Co I	3	1.66	0.05	−3.33	0.05	Co I	3	1.51	0.13	−3.48	0.11
Ni I	1	2.71	0.15	−3.51	−0.13	Ni I	2	2.41	0.06	−3.81	−0.22
Zn I	1	1.73	0.25	−2.83	0.55	Zn I	1	< 1.57	...	< −2.99	< 0.60
Sr II	1	−2.31	0.15	−5.18	−1.81	Sr II	2	−2.13	0.15	−5.00	−1.41
Ba II	1	−3.20	0.15	−5.38	−2.01	Ba II	3	−2.26	0.15	−4.44	−0.85
Eu II	1	Eu II	1	< −2.77	...	< −3.29	< 0.31

For Zn, upper limits were determined from the line at 4810 Å. For Eu, they were derived from the line at 4129 Å.

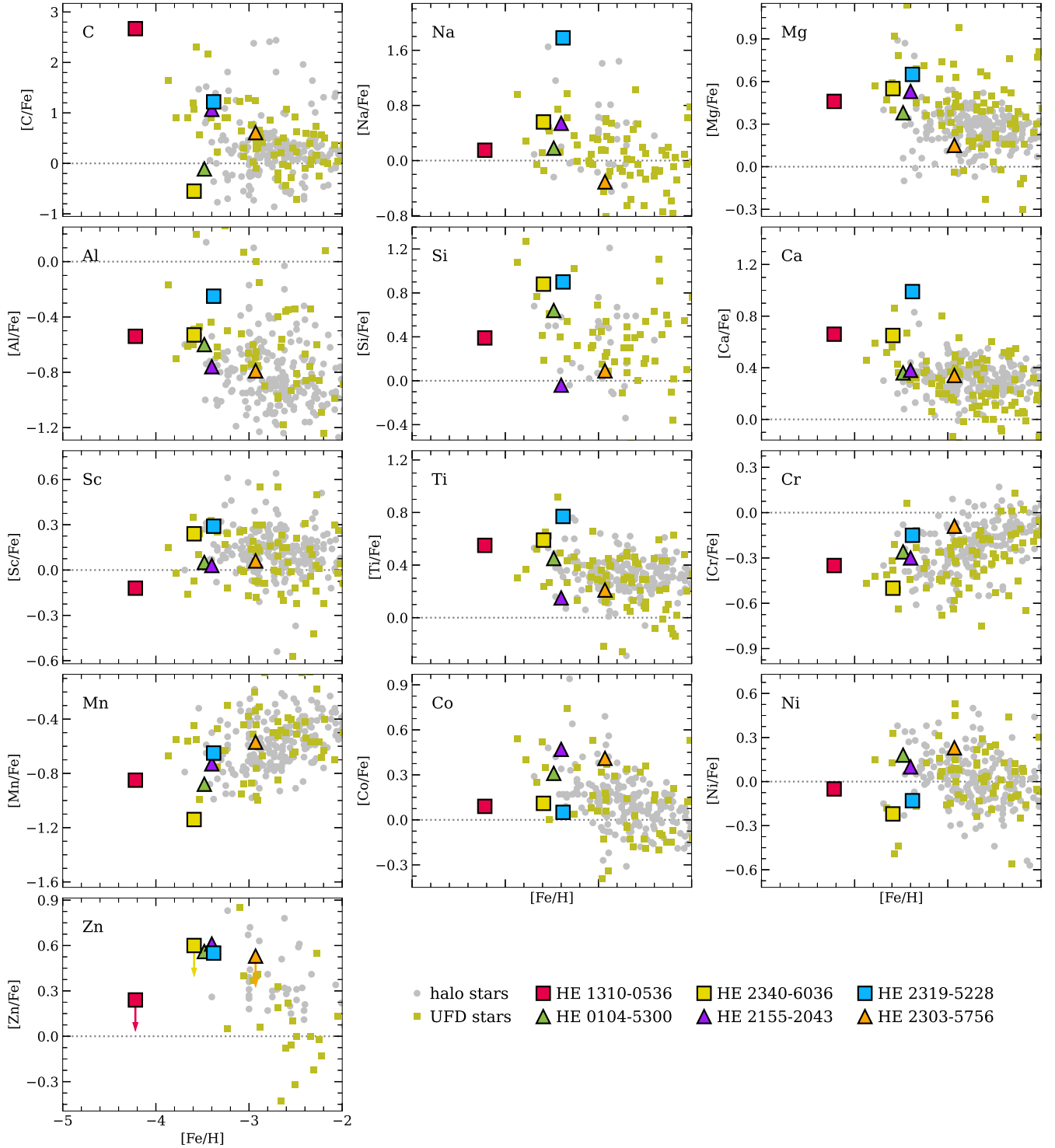


Figure 2. Light element abundances for our program stars (squares and triangles with black outlines), UFD stars (olive squares; see Section 4 for references), and halo stars (gray points; Cayrel et al. 2004; Barklem et al. 2005; Yong et al. 2013). The abundances of the stars denoted by triangles (HE 0104–5300, HE 2155–2043, HE 2303–5756) generally follow the abundance trends found in halo stars. Meanwhile, the stars denoted by squares (HE 1310–0536, HE 2340–6036, HE 2319–5228) show more variation and deviations from the general halo trend.

stars. This telling distinction between the two halves of our sample stars, as shown in Figure 3, suggests that three of our stars are similar to stars in UFDs (hence the square symbols) while the other three are similar to typical halo stars (hence the triangle symbols).

In line with our broader goal of building a set of metal-

poor halo stars that possibly originated from small satellite galaxies, we searched the literature for objects similar to our UFD star-like targets (square symbols in Figure 3). Using JINABase (Abomalima & Frebel 2018), we specifically looked for halo stars known to have low Sr abundances, specifically $[\text{Sr}/\text{H}] < -4.5$.

We found 61 of them (detailed in Table 9), which we added as orange diamonds to the bottom panel of Figure 3 (Li et al. 2015; Barklem et al. 2005; Roederer et al. 2014; Cayrel et al. 2004; Hansen et al. 2015; Lai et al. 2008; Placco et al. 2014a; Hollek et al. 2011; Jacobson et al. 2015; Cohen et al. 2013; Norris et al. 2007; Bonifacio et al. 2009; Ryan et al. 1996; Collet et al. 2006; Yong et al. 2013; Keller et al. 2014; Frebel et al. 2015; Caffau et al. 2011; Cohen et al. 2008; Frebel et al. 2007; Mardini et al. 2024). These panels are identical except for the addition of literature stars on the bottom panel. We opted to show these two datasets separately for clarity. Further discussion on the literature stars is presented in Section 6.

We then considered the overall abundance trends of Sr and Ba in various stars. We chose to focus on $[\text{Sr}/\text{H}]$ and $[\text{Ba}/\text{H}]$ values in our plots as these abundance ratios provide nucleosynthetically decoupled axes (as opposed to $[\text{Sr}/\text{Fe}]$ and $[\text{Ba}/\text{Fe}]$). For completeness, we nevertheless show $[\text{Sr}/\text{Fe}]$ and $[\text{Ba}/\text{Fe}]$ values. In Figure 4, we show our stars' Sr and Ba abundances, in comparison with a general set of metal-poor halo stars (gray points; same set as in Figure 2), with metal-poor stars in various UFDs (olive squares; same set as in Figure 2), and with the halo stars known to have low Sr abundances (orange diamonds; same set as in Figure 3).

In Figure 4, we keep the same shape grouping as derived in Figure 3 and explained in Section 4.3. For $[\text{Sr}/\text{H}]$, the square-denoted stars are clustered away from the triangle-denoted stars, lying at the bottom end of the overall trend set by halo stars. They also have slightly lower $[\text{Fe}/\text{H}]$ values than the triangle-denoted stars. However, for $[\text{Ba}/\text{H}]$, there is no separation between the two groups. They all cluster towards the lowest Ba abundances as set by the halo stars. As noted briefly in Section 4.2, the shape grouping also seems to correlate with light element abundances. We discuss this behavior further in Section 6.

We note for completeness that we detected no Eu lines in any of our stars but we provide upper limits in Table 5.

4.4 Abundance uncertainties

From our measurements of individual spectral lines for each element and the corresponding standard deviations σ , we calculated standard errors for each of our abundance measurements. However, for elements with a small number of lines ($2 < N < 30$), the resulting standard error will be underestimated. We thus applied small N corrections to arrive at our final values. We list our standard errors in Table 5. In several cases, however, the standard error was unrealistically small (< 0.05 dex). For these cases, we thus adopt a minimum nominal abundance uncertainty of 0.05 dex, a figure informed by the S/N and other typical uncertainties. For elements with only a single line detection, we estimated an uncertainty between 0.10 – 0.15 dex depending on the quality of the local spectrum and the S/N . Generally, our uncertainties range between 0.05 – 0.30 dex, reflecting the relatively good data quality. For elements without any line detections, we estimated their abundances with a 3σ upper limit, without including any uncertainty.

To determine the systematic uncertainties in our measurements, we varied each stellar parameter by its uncertainty to assess how the abundance changes in response to changes in stellar parameter values. We varied the effective temperature by 100 K, $\log g$ by 0.3 dex, and the microturbulence by 0.3 dex. We then recorded the change in abundance for each element. Our uncertainties are listed in Table 6 for HE 2155–2043 and HE 2303–5756, two example stars that illustrate this effect. The total uncertainties were found by adding all of the

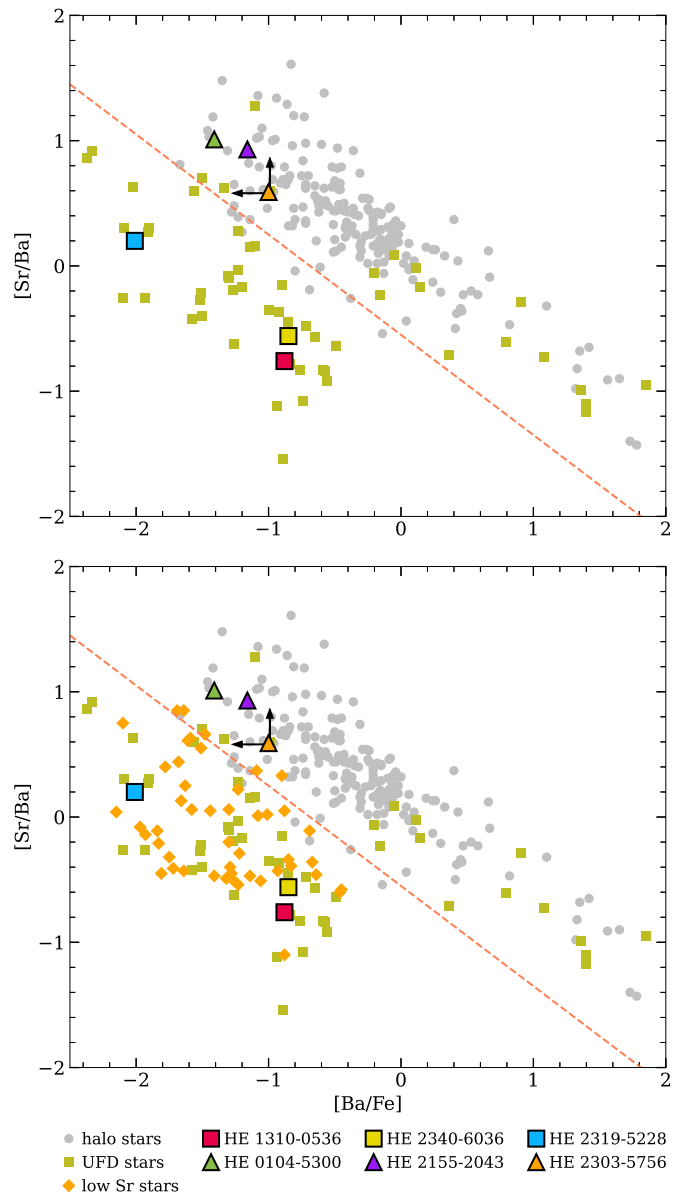


Figure 3. Top: $[\text{Sr}/\text{Ba}]$ vs $[\text{Ba}/\text{Fe}]$ for our sample stars in comparison with halo stars (gray points) and UFD stars (olive squares). The diagonal line guides the eye and separates halo stars from UFD stars. The UFD stars towards the bottom right corner that appear to extend the main halo trend are the highly r -process enhanced stars in Reticulum II (Ji et al. 2016a) as this is the region occupied by strongly enhanced r -process stars. Bottom: Same as above but with additional halo stars (orange diamonds) that have been selected with a Sr cut of $[\text{Sr}/\text{H}] < -4.5$. They appear to overlap with the region covered by UFD stars.

previously measured uncertainties in quadrature. Generally, the total uncertainties range from 0.10 to 0.30 dex.

4.5 Abundance comparison with literature values

In Table 7, we compare our abundance results with those from previous works that already analyzed our program stars. For HE 2155–2043, we compare our measurements with those from Purandardas & Goswami (2021) as well as the handful of measure-

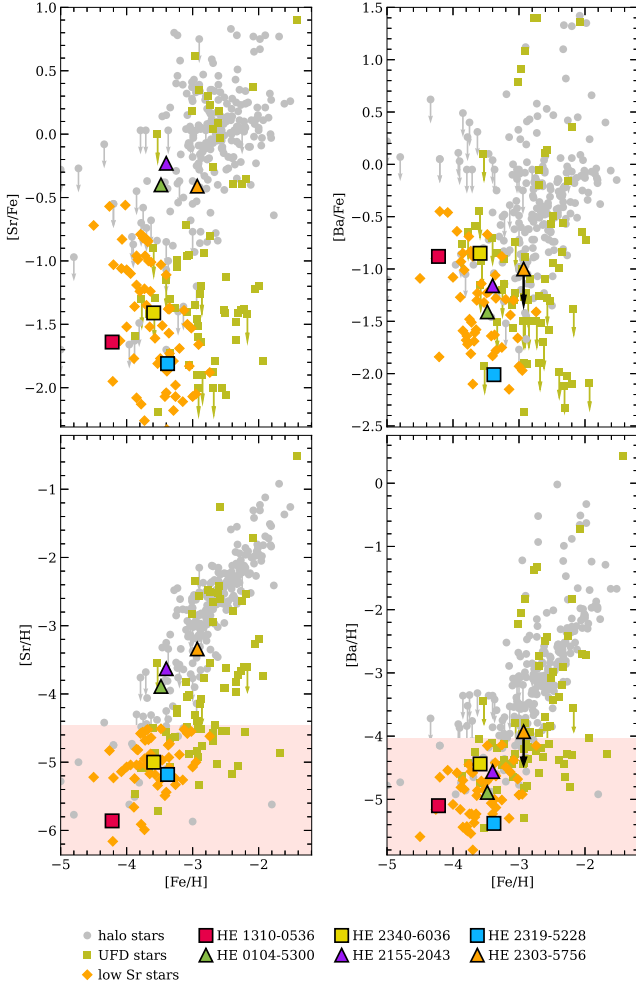


Figure 4. Sr and Ba abundances for our sample stars in comparison to halo stars (gray points), UFD stars (olive squares), and low Sr stars in the halo (orange diamonds). The program stars denoted by square symbols are those with $[\text{Sr}/\text{Ba}]$ and $[\text{Ba}/\text{Fe}]$ ratios similar to those of UFD stars. Meanwhile, the program stars denoted by triangles have halo-like $[\text{Sr}/\text{Ba}]$ and $[\text{Ba}/\text{Fe}]$ ratios. The pink-shaded regions on the bottom panels guide the eye to the lowest neutron-capture abundances (see Section 6.1 for discussion).

ments provided in Hansen et al. (2016b). For HE 0104–5300, we compare our results with those from Jacobson et al. (2015).

The manner in which each paper derived surface gravity varied, thus leading to differing numbers between this study and the others. This explains, for instance, the large discrepancy in $[\text{Mg}/\text{Fe}]$ between our work and Purandardas & Goswami (2021). There is also a significant difference in $[\text{C}/\text{Fe}]$, likely because we normalized the carbon G-band region of our respective spectra differently. We tested several different normalization schemes but we were not able to reproduce their reported value of $[\text{C}/\text{Fe}] \sim 2$. Meanwhile, Hansen et al. (2016b) reported $[\text{C}/\text{Fe}]$ for HE 2155–2043 and found a value closer to ours.

As for the comparison with Jacobson et al. (2015), our measurements for HE 0104–5300 agree reasonably well. Overall, for both stars, there is a moderate to good agreement between our results and the literature values at the 0.2 – 0.3 dex level.

Table 6. Example abundance uncertainties for HE 2155–2043 and HE 2303–5756

Species	Statistical Unc.	ΔT_{eff} [+100 K]	$\Delta \log(g)$ [+0.3 dex]	Δv_{mic} [+0.3 dex]	Total Unc.
HE 2155–2043					
C (CH)	0.10	−0.11	−0.12	0.01	0.19
Na I	0.21	0.09	−0.06	−0.15	0.27
Mg I	0.05	0.09	−0.07	−0.08	0.15
Al I	0.10	0.25	−0.07	−0.11	0.30
Si I	0.20	0.06	0.06	−0.13	0.25
Ca I	0.05	0.07	−0.03	−0.01	0.09
Sc II	0.05	0.06	0.08	−0.01	0.11
Ti I	0.08	0.12	−0.02	−0.01	0.15
Ti II	0.05	0.07	0.10	−0.06	0.14
Cr I	0.05	0.12	−0.02	−0.03	0.13
Mn I	0.15	0.16	0.02	−0.03	0.22
Fe I	0.05	0.12	−0.03	−0.08	0.16
Fe II	0.05	0.02	0.10	−0.01	0.11
Co I	0.05	0.09	−0.02	−0.07	0.13
Ni I	0.05	0.13	−0.05	−0.15	0.21
Zn I	0.21	0.07	0.05	0.01	0.23
Sr II	0.06	0.10	0.14	−0.27	0.32
Ba II	0.08	0.09	0.08	0.00	0.14
HE 2303–5756					
C (CH)	0.35	0.15	0.15	0.13	0.43
Na I	0.09	0.07	−0.01	0.01	0.11
Mg I	0.05	0.05	−0.03	0.00	0.08
Al I	0.05	0.02	0.00	0.01	0.05
Si I	0.15	0.10	0.00	0.00	0.18
Ca I	0.05	0.06	−0.01	0.01	0.08
Sc II	0.05	0.05	0.09	0.02	0.12
Ti I	0.05	0.08	−0.01	0.02	0.10
Ti II	0.05	0.05	0.08	0.00	0.11
Cr I	0.05	0.10	−0.01	0.02	0.11
Mn I	0.15	0.03	−0.07	−0.04	0.17
Fe I	0.05	0.08	−0.01	0.01	0.10
Fe II	0.05	0.02	0.11	0.01	0.12
Co I	0.05	0.09	−0.04	0.00	0.11
Ni I	0.05	0.13	−0.05	0.02	0.15
Sr II	0.06	−0.03	0.04	−0.05	0.09

5 KINEMATIC ANALYSIS

In addition to chemical abundances, we also use stellar kinematics to reconstruct each star’s orbital history and learn more about its origin scenario. We employ the same procedure detailed in Mardini et al. (2022a). The authors used *Gaia* astrometric data in combination with a time-varying Galactic potential modeled in The ORIENT⁴. The potential was constructed from snapshots of a large-scale cosmological simulation of a Milky Way-like halo (see Mardini et al. 2020 for more details).

For this work, we determined distances to our sample stars using data from *Gaia* DR3 (Gaia Collaboration et al. 2022). Despite *Gaia*’s unprecedented precision, a considerable number of its parallax measurements have large uncertainties such that distances derived by simply inverting the parallax ($d = \frac{1}{p}$) can be unreliable. To correct this, we adopt the method described in Mardini et al. (2022b) where we first employ a zero-point correction using a pseudocolor where available. We then probabilistically derive a final distance estimate using a space density prior, also in combination with the zero-point correction.

However, as Luri et al. (2018) recommended, distances should

⁴ Available at <https://github.com/Mohammad-Mardini/The-ORIENT>

Table 7. Comparisons with results from other studies

HE 2155–2043					
Species	Purandardas et al. 2021		Hansen et al. 2016	This Study	
	$\log \epsilon(X)$	[X/Fe]	[X/Fe]	$\log \epsilon(X)$	[X/Fe]
C (CH)	7.05	2.05	0.7	6.00	0.97
Na I	3.79	0.98	...	3.37	0.54
Mg I	5.74	1.57	...	4.72	0.53
Al I	2.29	-0.76
Si I	4.06	-0.04
Ca I	3.35	0.44	...	3.32	0.38
Sc II	-0.36	-0.02	...	-0.22	-0.03
Ti I	1.93	0.38
Ti II	1.67	0.21	...	1.70	0.15
Cr I	2.11	-0.10	...	1.93	-0.30
Mn I	2.04	0.04	...	1.29	-0.73
Fe I	4.07	0.00	0.00	4.10	0.00
Fe II	4.01	4.18	0.08
Co I	2.46	0.90	...	2.05	0.47
Ni I	3.09	0.30	...	2.92	0.10
Zn I	1.77	0.61
Sr II	-0.66	-0.04	0.2	-0.76	-0.23
Ba II	-2.95	-1.64	...	-2.38	-1.16
Eu II	< -2.50	<0.38

HE 0104–5300				
Species	Jacobson et al. 2015		This Study	
	$\log \epsilon(X)$	[X/Fe]	$\log \epsilon(X)$	[X/Fe]
C (CH)	4.77	0.13	4.77	-0.17
Na I	2.74	0.29	2.94	0.18
Mg I	4.37	0.57	4.50	0.38
Al I	2.06	-0.60	2.37	-0.60
Si I	4.65	0.93	4.67	0.64
Ca I	3.01	0.46	3.22	0.36
Sc II	-0.83	-0.19	-0.29	0.05
Ti I	1.37	0.21	1.74	0.27
Ti II	1.41	0.25	1.91	0.45
Cr I	1.39	-0.46	1.89	-0.26
Mn I	1.12	-0.52	1.07	-0.88
Fe I	3.71	0.00	4.02	0.00
Fe II	3.72	0.01	4.27	0.25
Co I	1.34	0.14	1.82	0.31
Ni I	2.30	-0.12	2.92	0.18
Zn I	1.64	0.56
Sr II	-1.71	-0.79	-1.02	-0.40
Ba II	-3.25	-1.64	-2.71	-1.41
Eu II	< -2.62	<0.34

ideally be derived using a full Bayesian approach. Following this suggestion, we thus infer a final distance measurement using the more rigorous probabilistic method described by [Bailer-Jones et al. \(2018\)](#). As such, we adopt an exponentially decreasing space density prior (SDP; as opposed to an isotropic prior) to calculate our final distance estimate. We then run a Monte Carlo simulation generating 10,000 realizations for each star and assuming a normal distribution centered around the corrected parallax and its standard deviation. The mean of the resulting posterior distribution is the final distance for each star. Our final distances are presented in Table 8.

We then calculate the positions and velocities of our sample stars using *Gaia* coordinates, proper motion, and radial velocity. We adopt a position of the Sun of $R_{\odot} = 8.178 \pm 0.013$ kpc away from the Milky Way’s center ([GRAVITY Collaboration et al. 2019](#)) at a vertical distance $z_{\odot} = 20.8 \pm 0.3$ pc above the Galactic plane and solar veloci-

ties as given by [Bennett & Bovy \(2019\)](#) and [Schönrich et al. \(2010\)](#). We adopt $V_{\text{LSR}} = 220 \text{ km s}^{-1}$ as measured by [Kerr & Lynden-Bell \(1986\)](#). Table 8 summarizes the kinematic parameters of our sample stars.

The strong retrograde V motions of all of our stars (i.e., $V < 0$), especially those of HE 2303–5756 and HE 2155–2043 with $V \sim -450 \text{ km s}^{-1}$, suggest that our sample is indeed composed of halo stars, a finding which aligns with their extremely metal-poor nature. These results suggest a possible early accretion origin of our stars. We also tested using $V_{\text{LSR}} = 232 \text{ km s}^{-1}$ ([McMillan 2017](#)) and $V_{\text{LSR}} = 238 \text{ km s}^{-1}$ ([Schönrich 2012](#)) to assess the impact of different V_{LSR} values on our conclusions regarding the origins of our stars. Using these new values changes V by only 10 km s^{-1} . Thus, changing V_{LSR} does not affect our conclusion regarding the retrograde motion of our stars.

Given all these inputs, we derive the Galactocentric coordinates (X, Y, Z) with a right-handed frame and rectangular Galactic velocities (U, V, W). With these kinematic parameters, we then back-integrate each star’s orbit with a time-varying Galactic potential, namely ORIENT potential #483868 ([Mardini et al. 2022a](#)). To investigate their orbits statistically, we generate 1,000 realizations of each star’s orbital evolution. In Figure 5, we show one such realization for our UFD star-like targets, namely HE 1310–0536, HE 2340–6036, and HE 2319–5228 (square symbols in relevant figures).

Of particular note is each star’s Z_{max} , its maximum distance above or below the Galactic plane. On the right column of Figure 5, we show the distribution of Z_{max} values over 1,000 realizations. In Table 8, we list our program stars’ median Z_{max} values. All of our program stars have significant Z_{max} , generally ranging between 7 – 48 kpc, once again confirming that these are halo stars. Many of them also have rather elliptical orbits about the Galactic Center.

For HE 1310–0536, we were unable to derive a reliable distance due to large uncertainties in the *Gaia* data ($d = 11.9 \pm 2.3$ kpc). To err on the side of caution, we thus carried out our kinematic analysis (described above) of HE 1310–0536 three times, with three possible distances taking into account its uncertainty (9, 12, and 14 kpc). This was to test the effects of the distance uncertainty on our orbital history results. We find that in all three cases, the star appears to be part of the halo, rather than the disk.

6 ON THE ORIGINS OF HALO STARS WITH LOW NEUTRON-CAPTURE ELEMENT ABUNDANCES

6.1 Small Accreted Stellar System (SASS) stars

In Figure 2, we showed that our six sample stars — all metal-poor and deficient in neutron-capture elements — generally follow the light element abundance trends set by typical halo stars. In Section 5, we also showed that all our stars have halo kinematics with a strong propensity for significantly retrograde orbits. Yet, when considering their [Sr/Ba] vs. [Ba/Fe] behavior (as shown in Figure 3), the sample splits into two distinct groups. Three stars fall in the region typically occupied by UFD stars, while the other three stars overlap with the main halo star branch. This division persists noticeably in the [Sr/H] vs. [Fe/H] panel in Figure 4. To some degree, this division is also seen in some of the light elements, particularly in Ca, Co, and Ni.

Generally, stars in UFDs have a strong tendency to cover regions of the lowest [Sr/H] and [Ba/H] values, i.e., [Sr/H] < -4.0 and [Ba/H] < -4.0 as shown in [Frebel et al. \(2014\)](#). To arrive at more stringent results, we restrict the following discussion to an even lower neutron-capture abundance cutoff at [Sr/H] < -4.5 and [Ba/H] < -4.0. These low Sr and Ba regions are colored pink in Figure 4 to guide the eye.

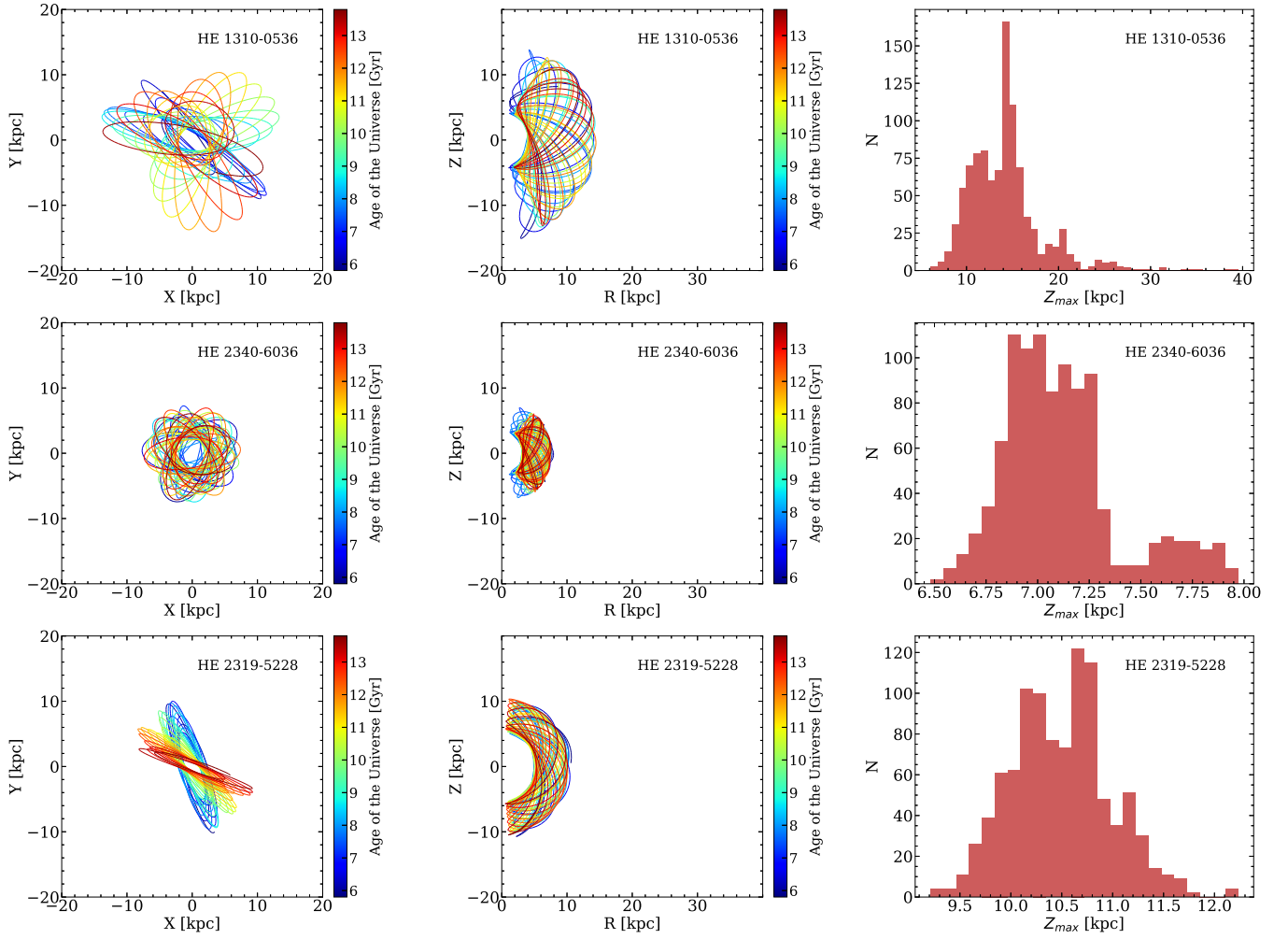


Figure 5. Orbital evolution over the last 8 billion years of our three UFD star-like targets. For every star, we show one realization of its orbital history, back-integrated using the time-dependent ORIENT potential #483868. Left: View of the Galactic plane from above in X-Y coordinates (in kpc). Center: Side view showing the Z height of the orbit as a function of distance from the Galactic Center. Right: Histogram showing the distribution of Z_{\max} (maximum distance above or below the Galactic plane) over 1000 realizations of the star’s orbital evolution.

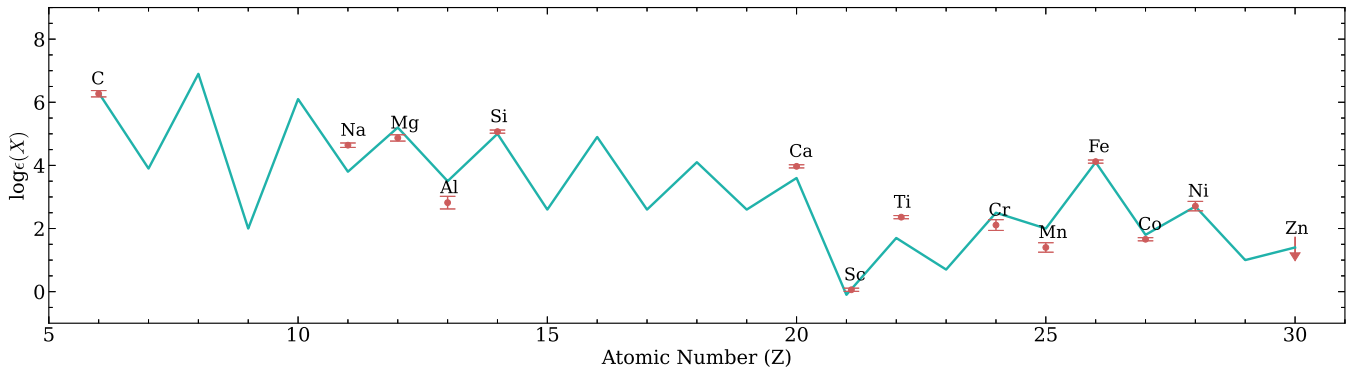


Figure 6. Abundances of HE 2319–5228 as a function of atomic number. Overlaid is a Starfit supernova nucleosynthesis model (teal line) that best matches the data (red points). Sc is not considered in the fit given uncertainties in the Sc production, as recommended by Starfit. Overall, the fit is moderate given that Cr and Mn are significantly overproduced by the model. It corresponds to a progenitor with ~ 27 solar masses and an explosion energy of 0.9 Bethe. Applying exemplary NLTE corrections to multiple elements did not significantly change the fitting outcome.

Table 8. Kinematic parameters of our sample stars

Star	X [kpc]	Y [kpc]	Z [kpc]	U [km s ⁻¹]	V [km s ⁻¹]	W [km s ⁻¹]	Distance [kpc]	Z_{\max} [kpc]
HE 0104–5300	-6.73	-2.81	-6.54	-177.98	-303.15	-117.25	7.4 ± 0.6	31
HE 1310–0536	-3.88	-4.60	9.51	-137.98	-263.95	64.35	11.9 ± 2.3	14
HE 2155–2043	-4.11	2.64	-5.81	-216.27	-467.79	-245.61	6.4 ± 1.2	48
HE 2303–5756	-7.65	-0.34	-0.86	-213.62	-430.29	155.35	1.1 ± 0.0	12
HE 2319–5228	-5.97	-1.25	-4.37	57.12	-190.84	-245.15	5.3 ± 0.4	11
HE 2340–6036	-6.10	-1.92	-4.02	124.93	-281.53	-60.58	5.6 ± 0.4	7

Indeed, half of our sample stars (denoted with squares for their UFD-like [Sr/Ba] vs. [Ba/Fe] behavior) fall in the pink low-Sr region in the [Sr/H] versus [Fe/H] panel of Figure 4. Meanwhile, the other three stars (denoted with triangles) do not. For the [Ba/H] versus [Fe/H] panel, however, all sample stars more or less cluster in the pink low-Ba region typically covered by UFD stars. All these stars are extremely metal-poor.

Altogether, the three characteristics of (1) low [Fe/H] values paired with a corresponding [Sr/Ba] value (as in Figure 3), (2) low [Sr/H] values, and (3) retrograde halo orbits suggest that three of our stars have origins extremely similar to those of typical UFD stars. This similarity implies that these stars (HE 2319–5228, HE 2340–6036, HE 1310–0536) may have originated from small dwarf galaxies long accreted by the Milky Way. On the other hand, the other three stars (HE 0104–5300, HE 2155–2043, HE 2303–5756) may have different origin scenarios. Perhaps they came from larger dwarf galaxies (analogous to the classical dwarf spheroidal galaxies) which underwent some amount of chemical evolution before eventually being accreted by the Galaxy. Their Sr and Ba behavior resembles that of several extant satellite systems (e.g., Venn et al. 2004).

Informed by the above arguments and by observations of stars in UFDs, we can now assume that stars with the lowest Fe and Sr values originated in some of the smallest, earliest systems that formed in the universe. We will refer to these stars (the low-Sr stars represented as squares in the various figures) as stars from Small Accreted Stellar Systems (SASS). Now we will go one step further and assume that if a star in the Galactic halo has an extraordinarily low Sr abundance, then it must also be a SASS star. As will be discussed later, we indeed find many such SASS stars in the literature. Together, these stars open up new ways of studying early star formation environments, the early assembly history of the Milky Way, and the population of the earliest galaxies.

In the following subsections (6.2, 6.3, 6.4, 6.5), we discuss the environments of early dwarf galaxies and establish that SASS stars indeed originated from such environments. In later subsections (6.6, 6.7), we discuss SASS stars in the literature and the broader potential of SASS stars as probes of the early universe.

6.2 Light element abundances

As noted in Subsection 4.2, SASS stars tend to show larger deviations from the well-established halo trends in their light element abundances — a behavior found repeatedly among the most iron-poor stars. These iron-poor stars are thought to have formed from gas that was enriched by individual and/or unusual supernova progenitors and/or gas that underwent inhomogeneous mixing (Christlieb et al. 2004; Frebel et al. 2005; Placco et al. 2015; Frebel & Norris 2015). This behavior offers principal support for our claim that SASS stars formed in the earliest systems; they experienced enrichment events that were individual and more stochastic.

6.3 Carbon abundances

Another feature of the most iron-poor stars is strong carbon enhancement. Two of our three SASS stars are strongly carbon-enhanced, with HE 2319–5228 having [C/Fe] = 1.2 and HE 1310–0536 having [C/Fe] = 2.7. Once again, this lends further support to our claim that SASS stars came from the earliest systems. However, our third SASS star, HE 2340–6036, has a low carbon abundance with [C/Fe] = -0.55. The origin of such a low value generally remains unclear, but it could be due to extreme inhomogeneous mixing.

Interestingly, stars in UFDs tend to have only mild carbon enhancement or even subsolar levels of carbon (Frebel et al. 2016; Norris et al. 2010). Only one of our SASS stars, HE 2340–6036, has UFD-like carbon abundance levels. Meanwhile, our other two SASS stars are grossly different in that they are much more carbon-enhanced. We note, however, that several individual UFD stars are known to have such extremely high carbon abundances (Lai et al. 2011). More data might help shed light on the overall C behavior in UFDs. In the meantime, we continue to assume that SASS stars are indeed not unlike the surviving UFD stars.

6.4 Supernova nucleosynthesis yields

We further test the idea of early pre-enrichment by considering supernova nucleosynthesis yields and how they match with the now-observed abundances in our SASS stars. We used Starfit⁵ (Heger & Woosley 2010), a fitting tool that matches the observed light element ($Z < 30$) abundance signatures with models of Pop III supernova nucleosynthesis yields. This provides clues to the properties of the (possibly Pop III) progenitors that operated in the birth environments of our SASS stars.

Studies of the ultra-faint dwarf galaxies Hercules and Leo IV suggest that they may have been enriched by the supernovae of putative Population III stars (Koch et al. 2008; Simon et al. 2010). We nominally find Pop III progenitor masses of 10 to 23 M_{\odot} and accompanying explosion energies of $\sim 10^{50}$ to 10^{51} ergs. An example fit is shown in Figure 6. As can be seen, the fit for HE 2319–5228 is overall of moderate quality. The same is true for the fits of other stars. These rather low explosion energies are in line with our claim that SASS stars formed in early systems. Otherwise, significantly larger energies might have blown the systems apart and prevented further star formation.

6.5 Neutron-capture element abundances

A remaining question pertains to the origins of low neutron-capture element abundances — a property shared by both UFD and SASS

⁵ Available at <https://starfit.org>

stars. Generally, low neutron-capture element abundances imply either (1) a limited production of said elements, or (2) a limited number of enrichment events in combination with poor mixing and distribution of metals. Possible options for events and processes include the limited r -process operating in supernovae (Wanajo & Ishimaru 2006; Arcones & Montes 2011; Frebel 2018) and other heavy element production processes associated with supernovae such as spin-stars (Maeder et al. 2015; Hansen et al. 2016a), all in concert with the commensurate carbon enhancement events. Crucially, we do not consider neutron star mergers as they would strongly overproduce neutron-capture elements, likely generating abundances higher than those observed in our SASS stars. Not only that, we found upper limits of $[\text{Eu}/\text{H}] < -3$ for five out of our six program stars. With such low Eu levels, we can reasonably exclude a rare, prolific r -process event such as a neutron star merger. Our low Eu levels are more in line with the Eu abundances found in typical UFDs.

Nevertheless, it is interesting to consider whether any SASS stars have a $[\text{Sr}/\text{Ba}]$ ratio similar to that produced by either the s - or the r -process. Typical r -process stars have $[\text{Sr}/\text{Ba}] \sim -0.4$ to -0.7 (Frebel & Ji 2023; Ji et al. 2016c) while s -process stars have $[\text{Sr}/\text{Ba}] < -1$. None of our stars has $[\text{Sr}/\text{Ba}] < -1$. However, one SASS star has $[\text{Sr}/\text{Ba}] = -0.87$ (HE 1310–0536) and another one has $[\text{Sr}/\text{Ba}] = -0.56$ (HE 2340–6036). These stars have extremely low levels of $[\text{Sr}/\text{H}]$ (-5.86 for HE 1310–0536; -5.00 for HE 2340–6036) and $[\text{Ba}/\text{H}]$ (-5.10 for HE 1310–0536; -4.44 for HE 2340–6036). This suggests the potential existence of early r -process nucleosynthesis, or at least, a dilution process that led to such low overall levels. Perhaps this nucleosynthetic event was associated with an early supernova such as a magnetorotational hypernova (Yong et al. 2021). More observations of similar stars could help shed light on this question, which we address further below. For completeness, we note that the third SASS star, HE 2319–5228, has $[\text{Sr}/\text{Ba}] = 0.2$. Its neutron-capture elements likely have a different origin.

6.6 SASS stars in the literature

As we established in the previous subsections, our three SASS stars likely originated in the earliest systems in the universe. A large set of such stars would therefore allow us to study in detail the early environments of dwarf galaxies. Motivated by this, we sought to expand our collection of 3 SASS stars by searching the literature for similar stars. To this end, we queried JINAbase for stars with low $[\text{Fe}/\text{H}]$ and $[\text{Sr}/\text{H}] < -4.5$. We found 61 such stars which we show as orange diamonds in Figures 3, 4, and 7. These literature SASS stars are listed in Table 9 together with selected chemical abundances, JINAbase identification numbers, and radial velocities.

In Figure 4, our literature SASS stars lie within the low-Sr region of the $[\text{Sr}/\text{H}]$ versus $[\text{Fe}/\text{H}]$ plot. This is expected since we selected these stars precisely for their having $[\text{Sr}/\text{H}] < -4.5$. Though these stars were only selected for their low $[\text{Sr}/\text{H}]$, it is interesting to note that these same stars strictly have low barium abundances; they all have $[\text{Ba}/\text{H}] < -4.0$. This makes SASS stars generally straightforward to identify using neutron-capture element abundances. However, while a low $[\text{Ba}/\text{H}]$ value is a necessary characteristic for a SASS star, this criterion by itself is not sufficient for the selection of SASS stars. In addition to being poor in Sr (and by extension, Ba), SASS stars must also have low metallicities, i.e., $[\text{Fe}/\text{H}] \sim -5.0$ to -3.0 . This low-metallicity criterion selects for stars that formed in the early universe.

Now we consider the reverse logical path. Looking at their $[\text{Sr}/\text{Ba}]$ ratio in Figure 3, all these literature SASS stars fall into the UFD region (just as our three program SASS stars). In Figure 7, we show

the light element abundances of these stars (with abundances as collected from JINAbase). Like our three program SASS stars, the literature SASS stars have a tendency to be more scattered in their light element abundances, compared to the typical halo trend set by stars with higher Sr values. This behavior was foreshadowed by our program SASS stars and is more apparent now with the literature SASS stars. We note that as more stars become available, a more detailed analysis of the overall behavior would deliver more accurate results.

Finally, we carried out the same kinematic analysis detailed in Section 5 on the literature SASS stars to assess their orbital histories. Like our program SASS stars, we find a strong tendency for these stars to be on highly retrograde orbits, with essentially no prograde motion present.

6.7 Studying the early universe with SASS stars

We thus conclude that halo stars with $[\text{Sr}/\text{H}] < -4.5$ can be considered SASS stars and that they likely originated from early small systems that were accreted by the Milky Way at the earliest times. After all, the early Milky Way assembled from galactic building block-type systems much like UFDs. Thus it should not be surprising that at least the low-mass stars are still present in our Galaxy and that we can observe them. Accordingly, we suggest using $[\text{Sr}/\text{H}] < -4.5$ as an important selection tool in identifying the truly oldest stars, namely the SASS stars, in our Galaxy. Furthermore, these stars will be characterized by a suitable UFD-like $[\text{Sr}/\text{Ba}]$ ratio (together with an appropriate $[\text{Ba}/\text{Fe}]$ value), as well as a highly retrograde orbit.

From the chemical abundances of SASS stars, it appears that the earliest systems accreted by the Milky Way were enriched by a very small number of supernovae whose (perhaps unique) yields were somewhat inhomogeneously mixed. This inhomogeneity produced variations in light element abundances, including carbon abundances, from system to system. Neutron-capture elements were sparsely produced and/or diluted likely in multiple ways, with r -process nucleosynthesis (at least up to Ba) playing a role. This suggests that most, if not all, elements were produced in small amounts from the earliest times onward. High-resolution cosmological simulations of early (baryonic) structure formation may be able to more fully model the population of the earliest galaxies and building blocks based on these observational constraints.

Tracing the oldest surviving stars within large galaxies, such as the Milky Way, would be another avenue towards confirming our observational findings that there appears to be a significant population of the very oldest stars present in the halo. Adding the Sr abundance as a criterion in addition to the commonly used Fe abundance may finally offer a path towards identifying not just the most metal-poor but indeed the oldest stars in the universe.

We note that SASS stars may not be the only unique survivors of this very early time. For instance, stars with slightly higher Sr values may well be part of this extremely ancient population. However, we apply a more stringent cut here in this work to ensure the selection of a relatively clean and easily identifiable representative set of this unique population of the very oldest stars in the universe.

Going forward, SASS stars offer a new path to identifying ancient stars that are relatively close by. These nearby stars, which are easier to observe than the faint and distant dwarf galaxy stars, will allow for more detailed probing of early galactic environments and the galaxy formation era. With many more halo stars available to probe early star formation, we may eventually be able to establish the full history of the systems that built the Milky Way. In addition, we may better

understand the conditions of the earliest galaxies which hosted the oldest and most metal-poor stars.

7 SUMMARY

In this paper, we studied a sample of metal-poor stars with low neutron-capture element abundances to gain insight into the origins of each of our program stars, and to investigate the potential connections of these halo stars to those in present-day UFDs and other dwarf galaxies. Our findings can be broadly summarized as follows:

(i) High-resolution optical spectra of our target stars were obtained with Magellan/MIKE. Stellar parameters (T_{eff} , $\log g$, and v_{mic}) were determined as part of performing a detailed chemical abundance analysis. Depending on the element, we obtained abundances using either equivalent widths or spectrum synthesis. We obtained abundances of a total of 17 light and heavy elements. All our stars were found to have $[\text{Fe}/\text{H}]$ between -2.9 and -4.3 .

(ii) The abundances of our six stars generally agree well with halo trends for most elements. However, for some elements (specifically Al, Ca, Ti, Co, Ni), our three low-Sr stars ($[\text{Sr}/\text{H}] < -4.5$; namely HE 1310–0536, HE 2340–6036, HE 2319–5228) show larger scatter and deviations from the main halo trend. In addition, two of our stars (HE 2340–6036 and HE 0104–5300) have C abundances that are far below average.

(iii) The Sr and Ba abundances of our stars are extremely low, with our low-Sr program stars (square symbols in relevant figures) having values of $[\text{Sr}/\text{H}] < -4.5$ and $[\text{Ba}/\text{H}] < -4.0$. In terms of neutron-capture abundances, these three stars are highly similar to UFD stars (see Figures 3 and 4). The other three program stars (triangle symbols in relevant figures) are separated in a distinct cluster in chemical abundance space, following the general halo trend set by higher-metallicity stars.

Interestingly, this separation does not exist for Ba abundances, with all six program stars having $[\text{Ba}/\text{H}] \lesssim 4.0$, and following the main trend. Therefore, Sr abundance is a telling sign of whether a star is similar to a UFD star, and by extension, old.

(iv) The low-Sr program stars (square symbols in relevant figures) possess $[\text{Sr}/\text{Ba}]$ ratios that do not reflect the main halo trend, but instead fall into the regime of UFD stars (see Figure 3). We identify these three stars as having similar origins to the metal-poor stars observed in UFDs. We label these stars, and others with similarly low $[\text{Sr}/\text{H}]$ values, as "SASS" stars. SASS stars are named as such because they likely originated in the early universe from Small Accreted Stellar Systems. Since these SASS stars are nearer to us compared to the very faint stars in surviving UFDs, identifying them in the halo allows for more detailed studies of accreted systems.

(v) From a kinematic analysis, we found that all program stars had extremely large and retrograde V velocities. This retrograde motion is indicative of objects that were accreted by the Milky Way rather than formed within it. This supports our conclusion that the stars with the lowest Sr and Ba abundances are likely some of the earliest accreted objects.

(vi) We searched the literature for additional SASS stars using the $[\text{Sr}/\text{H}] < -4.5$ cut and found 61 more such stars in the halo. A significant fraction of stars with $[\text{Fe}/\text{H}] < -3$ show these very low neutron-capture abundances. This fact supports the idea that the most metal-poor stars are also the oldest stars in our Galaxy (or at least the earliest stars that were accreted by the proto-Galaxy).

(vii) The population of SASS stars is easily identifiable with low Fe and Sr abundances. This easy identification of ancient stars will ultimately allow insights into the earliest star-forming environments,

the origins and histories of the surviving UFDs, as well as the earliest assembly phase of the Milky Way.

(viii) The earliest systems were likely enriched by a very small number of supernovae whose yields were somewhat inhomogeneously mixed. This produced variations in light element abundances, including carbon abundances, from system to system. Neutron-capture elements were sparsely produced and/or diluted likely in different ways, with r -process nucleosynthesis playing a role.

Indeed, UFDs offer insights into the conditions of the early universe. In particular, they provide glimpses into early star formation environments, early chemical enrichment events, and even the earliest phases of the Milky Way's formation. However, their limited number of observationally accessible stars naturally limits their further exploration. Now, SASS stars may fill that gap and provide a new important line of access to the early cosmos. These stars, which now lurk in the Galactic halo, may shed further light on the nature and origins of the oldest stars in the universe.

ACKNOWLEDGEMENTS

HDA, ASF, and CGF gratefully acknowledge support from the MIT Undergraduate Research Opportunities Program Office. AF acknowledges support from NSF grants AST-1716251 and AST-2307436. MKM and AF acknowledge partial support from NSF grant OISE 1927130 (International Research Network for Nuclear Astrophysics/IReNA).

This work has made use of data from the European Space Agency (ESA) mission *Gaia* (<https://www.cosmos.esa.int/gaia>), processed by the *Gaia* Data Processing and Analysis Consortium (DPAC, <https://www.cosmos.esa.int/web/gaia/dpac/consortium>). Funding for the DPAC has been provided by national institutions, in particular the institutions participating in the *Gaia* Multilateral Agreement. This work made use of NASA's Astrophysics Data System Bibliographic Services. This research has made use of the SIMBAD database, operated at CDS, Strasbourg, France. This work made use of Astropy:⁶ a community-developed core Python package and an ecosystem of tools and resources for astronomy (Astropy Collaboration et al. 2013, 2018, 2022).

This work made use of general-purpose Python libraries, namely NUMPY (Harris et al. 2020), MATPLOTLIB (Hunter 2007), PANDAS (Wes McKinney 2010), and SCIPY (Virtanen et al. 2020).

DATA AVAILABILITY

The individual line measurements are provided as supplementary material. The reduced spectra can be obtained by reasonable request to the corresponding author.

REFERENCES

- Abohalima A., Frebel A., 2018, *ApJS*, **238**, 36
 Aoki W., Beers T. C., Christlieb N., Norris J. E., Ryan S. G., Tsangarides S., 2007, *ApJ*, **655**, 492
 Applebaum E., Brooks A. M., Christensen C. R., Munshi F., Quinn T. R., Shen S., Tremmel M., 2021, *ApJ*, **906**, 96

⁶ <http://www.astropy.org>

Table 9. SASS stars from the literature

Name	[Fe/H]	[C/H]	[Mg/H]	[Sr/H]	[Ba/H]	JINAbase ID	RV	Reference
HE 2248–3345	–2.74	–2.55	–2.82	–4.62	–4.15	901	145.4	BAR05
HE 2249–1704	–2.95	–3.18	–2.75	–5.00	–4.92	2604	–134.1	COH13
CS29502-042	–3.00	–2.94	–2.98	–5.07	–4.93	842	–138.05	CAY04
HE 2304–4153	–3.02	–3.71	–2.94	–4.55	–4.68	913	–221.7	BAR05
HE 0411–5725	–3.08	–2.61	–2.75	–4.58	–4.38	2557	286.1	COH13
HE 0316+0214	–3.13	–3.89	–2.49	–4.52	–4.57	268	–161.0	BAR05
BS16084-160	–3.15	–3.23	–3.01	–5.26	–5.30	638	–132.32	LAI08
HE 1416–1032	–3.20	< –3.51	–3.04	–4.89	–4.49	2623	5.2	COH13
CS22943–137	–3.22	N/A	–2.59	< –4.62	< –3.70	709	–20.0	RYA96
CD –24°17504	–3.23	–1.83	–2.84	–4.75	–4.15	3936	136.4	MAR24
LAMOST J0006+1057	–3.26	–3.58	–2.59	–5.33	–5.01	40	–281.6	LI15a
SMSS J031556.09–473442.1	–3.26	–3.07	–2.78	–5.24	–4.14	2372	192.3	JAC15
HE 0008–3842	–3.35	–4.26	–3.02	–4.73	–5.13	47	128.9	BAR05
HE 0344–0243	–3.35	–3.32	–2.95	–5.08	–4.63	2647	–110.5	COH13
SMSS J003327.36–491037.9	–3.36	< –3.76	–2.81	–4.93	–4.42	2351	84.7	JAC15
CS22949-048	–3.37	–3.38	–3.15	–4.75	–5.00	925	–160.8	ROE14b
CS30492-016	–3.40	–2.65	–2.62	< –5.10	< –3.33	1453	46.0	ROE14b
CS30325-094	–3.40	–3.21	–2.94	–5.44	–5.23	596	–138.0	CAY04
SMSS J023147.96–575341.7	–3.42	–3.07	–3.13	–5.49	–5.06	1923	219.2	JAC15
HE 0139–2826	–3.46	–2.98	–2.90	–4.97	–4.68	2022	–253	PLA14a
HE 1347–1025	–3.48	–3.21	–3.08	–4.51	–4.15	2622	48.6	COH13
HE 1356–0622	–3.49	–3.41	–2.93	–5.26	–4.72	2631	93.5	COH13
CS22942-002	–3.53	–3.26	–3.05	–5.34	–4.85	99	–155.0	ROE14b
SMSS J085924.06–120104.9	–3.63	–3.83	–3.02	–4.64	–4.86	2387	–187.6	JAC15
SDSS J1322+0123	–3.64	–3.15	–3.39	–4.88	–4.94	2263	105.0	PLA15a
LAMOST J0126+0135	–3.57	–4.08	–3.15	–5.18	–4.71	173	–256.0	LI15a
SMSS J184825.29–305929.7	–3.65	–3.40	–3.15	–5.17	–5.23	2471	110.2	JAC15
HE 2318–1621	–3.67	–3.13	–3.47	–4.67	–5.28	2080	–39.95	PLA14a
CS22952–015	–3.68	–4.52	–3.57	–4.52	–5.37	968	–7.0	ROE14b
HE 0302–3417a	–3.70	–3.22	–3.15	–5.05	–5.80	2026	121.7	HOL11
HE 2331–7155	–3.70	–2.34	–2.48	–4.53	–4.58	2082	210.6	HAN15
HE 0056–3022	–3.72	–3.52	–3.39	–4.68	–5.23	1490	29.7	ROE14b
HE 0926–0546	–3.73	< –3.11	–3.41	–4.95	–4.56	2637	152.9	COH13
HE 1116–0634	–3.73	–3.65	–2.91	–5.99	–5.54	2507	116.09	HOL11
HE 0048–6408	–3.75	–4.03	–3.35	–4.57	–5.23	2018	–33.99	PLA14a
HE 1012–1540	–3.76	–1.77	–2.36	–4.56	–4.45	392	225.6	ROE14b
CS22960–048	–3.78	–3.44	–3.19	–5.91	–5.50	815	–85.0	ROE14b
SMSS J010651.91–524410.5	–3.79	–3.66	–3.23	–4.58	–5.43	2355	189.5	JAC15
CS30339–073	–3.80	–3.73	–3.48	–5.04	–5.48	1451	171.0	ROE14b
BS16076–006	–3.81	–3.35	–3.25	< –5.30	< –4.86	474	203.12	BON09
SMSS J004037.56–515025.2	–3.83	–3.92	–3.24	–4.82	–4.84	2352	72.9	JAC15
CS22189–009	–3.85	–3.62	–3.48	–4.81	–5.44	222	–42.0	ROE14b
CS22963–004	–3.85	–3.58	–3.51	–5.04	–4.70	236	294.4	ROE14b
CS22891–200	–3.88	–3.53	–3.24	–5.24	–4.81	671	137.7	ROE14b
HE 1300+0157	–3.88	–2.54	–3.50	< –5.51	< –4.74	2665	73.4	FRE07a
SMSS J184226.25–272602.7	–3.89	< –4.18	–3.27	–5.66	–5.16	2469	–247.0	JAC15
HE 0945–1435	–3.90	< –1.87	–3.76	< –4.77	< –3.87	2035	121.8	HAN15
HE 1201–1512	–3.92	–2.72	–3.66	< –4.73	< –3.81	2040	237.2	YON13
SMSS J005953.98–594329.9	–3.94	–2.73	–3.32	–5.04	–4.58	2353	375.3	JAC15
HE 1424–0241	–3.96	< –3.17	–3.57	< –5.62	–4.92	2646	59.8	COH08
CS22172–002	–4.00	–3.77	–3.68	–5.07	–5.08	257	255.0	CAY04
HE 0057–5959	–4.08	–3.22	–3.57	–5.14	–4.54	2019	375.3	YON13
HE 2239–5019	–4.20	< –2.45	–3.70	< –4.75	< –4.15	893	368.7	HAN15
CS22885–096	–4.21	–3.81	–3.57	–6.16	–6.05	701	–249.1	ROE14b
BD+44° 493	–4.26	–3.08	–3.39	–4.83	–5.16	1192	–150.6	ROE14b
SDSS J102915.14+172927.9	–4.73	< –3.68	–4.70	< –5.00	...	2554	–34.5	CAF11a
CD –38° 245	–4.50	< –4.78	–3.93	–5.22	–5.59	1509	46.4	ROE14b
HE 0557–4840	–4.80	–3.14	–4.57	< –5.77	< –4.73	368	211.94	NOR07
SD1313–0019	–5.00	–2.04	–4.56	< –5.28	< –4.78	2262	267.0	FRE15
HE 0107–5240	–5.28	–1.58	–5.13	< –5.80	< –4.46	2021	44.78	CHR04
SMSS J031300.36-670839.3	< –7.30	–2.40	–4.30	< –6.70	< –6.10	2136	–67.93	KEL14
HE 2319–5228	–3.38	–2.16	–2.73	–5.18	–5.38		292.8	this study
HE 2340–6036	–3.59	–4.16	–3.04	–5.00	–4.44		212.4	this study
HE 1310–0536	–4.22	–2.18	–3.76	–5.86	–5.10		188.3	this study

References are as follows: LI15a: Li et al. (2015), BAR05: Barklem et al. (2005), ROE14b: Roederer et al. (2014), CAY04: Cayrel et al. (2004), HAN15: Hansen et al. (2015), LAI08: Lai et al. (2008), PLA14a: Placco et al. (2014a), HOL11: Hollek et al. (2011), JAC15: Jacobson et al. (2015), COH13: Cohen et al. (2013), NOR07: Norris et al. (2007), BON09: Bonifacio et al. (2009), RYAN96: Ryan et al. (1996), COL06: Collet et al. (2006), YON13: Yong et al. (2013), KEL14: Keller et al. (2014), FRE15: Frebel et al. (2015), CAF11a: Caffau et al. (2011), COH08: Cohen et al. (2008), FRE07a: Frebel et al. (2007), MAR24: Mardini et al. (2024)

Arcones A., Montes F., 2011, *ApJ*, **731**, 5
 Asplund M., Grevesse N., Sauval A. J., Scott P., 2009, *ARA&A*, **47**, 481
 Astropy Collaboration et al., 2013, *A&A*, **558**, A33
 Astropy Collaboration et al., 2018, *AJ*, **156**, 123
 Astropy Collaboration et al., 2022, *ApJ*, **935**, 167
 Bailer-Jones C. A. L., Rybizki J., Fousneau M., Mantelet G., Andrae R., 2018, *AJ*, **156**, 58

Barklem P. S., et al., 2005, *A&A*, **439**, 129
 Bennett M., Bovy J., 2019, *MNRAS*, **482**, 1417
 Bernstein R., Shectman S. A., Gunnels S. M., Mochnacki S., Athey A. E., 2003, *Proc. SPIE*, **4841**, 1694
 Bonifacio P., et al., 2009, *A&A*, **501**, 519
 Brandt T. D., 2016, *ApJ*, **824**, L31
 Brauer K., Andales H. D., Ji A. P., Frebel A., Mardini M. K., Gómez F. A.,

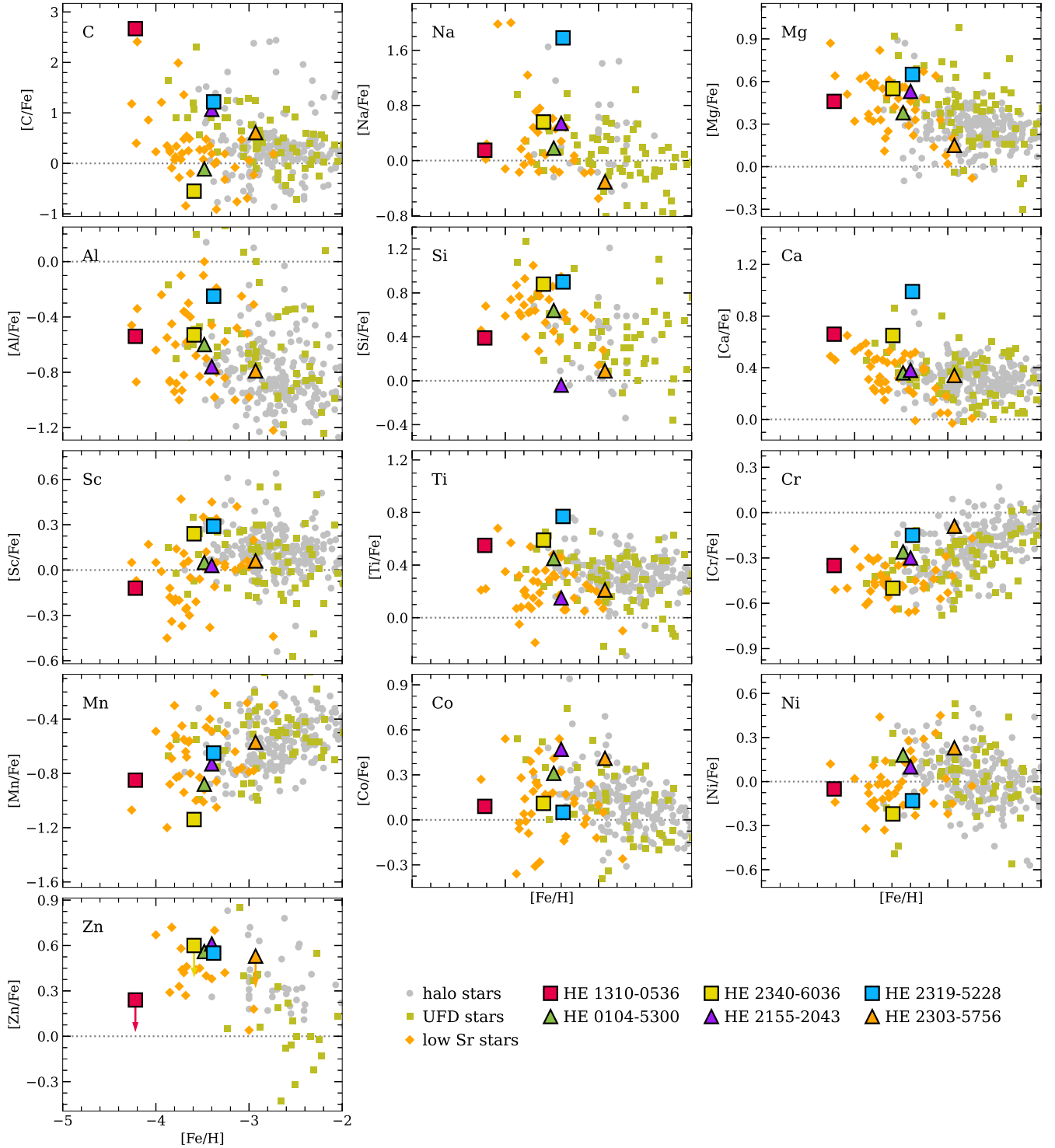


Figure 7. Same as Figure 2 but with halo stars having low $[Sr/H] < -4.5$ added as orange diamonds. While the metallicity is lower for those stars, the scatter is larger than that for the other halo stars. See Section 6.6 for discussion.

O’Shea B. W., 2022, *ApJ*, 937, 14
 Brown T. M., et al., 2012, *ApJ*, 753, L21
 Brown T. M., et al., 2014, *ApJ*, 796, 91
 Caffau E., et al., 2011, *Nature*, 477, 67
 Calabrese E., Spergel D. N., 2016, *MNRAS*, 460, 4397
 Casagrande L., Ramírez I., Meléndez J., Bessell M., Asplund M., 2010, *A&A*, 512, A54

Casey A. R., 2014, PhD thesis, Australian National University, Canberra
 Castelli F., Kurucz R. L., 2004, *A&A*, 419, 725
 Cayrel R., et al., 2004, *A&A*, 416, 1117
 Cescutti G., Chiappini C., Hirschi R., Meynet G., Frischknecht U., 2013, *A&A*, 553, A51
 Chiappini C., Hirschi R., Meynet G., Ekström S., Maeder A., Matteucci F., 2006, *A&A*, 449, L27

- Chiti A., Frebel A., Ji A. P., Jerjen H., Kim D., Norris J. E., 2018, *ApJ*, **857**, 74
- Chiti A., et al., 2021, *Nature Astronomy*, **5**, 392
- Chiti A., Simon J. D., Frebel A., Pace A. B., Ji A. P., Li T. S., 2022, *ApJ*, **939**, 41
- Chiti A., et al., 2023, *AJ*, **165**, 55
- Christlieb N., et al., 2004, *A&A*, **428**, 1027
- Cohen J. G., Christlieb N., McWilliam A., Shtetman S., Thompson I., Melendez J., Wisotzki L., Reimers D., 2008, *ApJ*, **672**, 320
- Cohen J. G., Christlieb N., Thompson I., McWilliam A., Shtetman S., Reimers D., Wisotzki L., Kirby E., 2013, *ApJ*, **778**, 56
- Collet R., Asplund M., Trampedach R., 2006, *ApJ*, **644**, L121
- François P., Monaco L., Bonifacio P., Moni Bidin C., Geisler D., Sbordone L., 2016, *A&A*, **588**, A7
- Frebel A., 2010, *Astronomische Nachrichten*, **331**, 474
- Frebel A., 2018, *Annual Review of Nuclear and Particle Science*, **68**, 237
- Frebel A., Bromm V., 2012, *ApJ*, **759**, 115
- Frebel A., Ji A. P., 2023, *arXiv e-prints*, p. [arXiv:2302.09188](https://arxiv.org/abs/2302.09188)
- Frebel A., Norris J. E., 2015, *ARA&A*, **53**, 631
- Frebel A., et al., 2005, *Nature*, **434**, 871
- Frebel A., et al., 2006, *ApJ*, **652**, 1585
- Frebel A., Johnson J. L., Bromm V., 2007, *MNRAS*, **380**, L40
- Frebel A., Kirby E. N., Simon J. D., 2010a, *Nature*, **464**, 72
- Frebel A., Simon J. D., Geha M., Willman B., 2010b, *ApJ*, **708**, 560
- Frebel A., Simon J. D., Kirby E. N., 2014, *ApJ*, **786**, 74
- Frebel A., Chiti A., Ji A. P., Jacobson H. R., Placco V. M., 2015, *ApJL*, **810**, L27
- Frebel A., Norris J. E., Gilmore G., Wyse R. F. G., 2016, *ApJ*, **826**, 110
- GRAVITY Collaboration et al., 2019, *A&A*, **625**, L10
- Gaia Collaboration et al., 2022, *arXiv e-prints*, p. [arXiv:2208.00211](https://arxiv.org/abs/2208.00211)
- Gilmore G., Norris J. E., Monaco L., Yong D., Wyse R. F. G., Geisler D., 2013, *ApJ*, **763**, 61
- Griffen B. F., Ji A. P., Dooley G. A., Gómez F. A., Vogelsberger M., O'Shea B. W., Frebel A., 2016, *ApJ*, **818**, 10
- Hansen T., et al., 2014, *ApJ*, **787**, 162
- Hansen T. T., Andersen J., Nordström B., Beers T. C., Yoon J., Buchhave L. A., 2015, *A&A*, **583**, A49
- Hansen T. T., Andersen J., Nordström B., Beers T. C., Placco V. M., Yoon J., Buchhave L. A., 2016a, *A&A*, **588**, A3
- Hansen C. J., et al., 2016b, *A&A*, **588**, A37
- Hansen T. T., et al., 2020, *ApJ*, **897**, 183
- Harris C. R., et al., 2020, *Nature*, **585**, 357
- Heger A., Woosley S. E., 2010, *ApJ*, **724**, 341
- Hirschi R., 2006, in Kubono S., Aoki W., Kajino T., Motobayashi T., Nomoto K., eds, *American Institute of Physics Conference Series Vol. 847, Origin of Matter and Evolution of Galaxies*. pp 71–76 ([arXiv:astro-ph/0601498](https://arxiv.org/abs/astro-ph/0601498)), doi:10.1063/1.2234385
- Hollek J. K., Frebel A., Roederer I. U., Sneden C., Shetrone M., Beers T. C., Kang S.-j., Thom C., 2011, *ApJ*, **742**, 54
- Holmbeck E. M., et al., 2020, *ApJS*, **249**, 30
- Hunter J. D., 2007, *Computing in Science & Engineering*, **9**, 90
- Ishigaki M. N., Aoki W., Arimoto N., Okamoto S., 2014, *A&A*, **562**, A146
- Jacobson H. R., et al., 2015, *ApJ*, **807**, 171
- Ji A. P., Frebel A., Chiti A., Simon J. D., 2016a, *Nature*, **531**, 610
- Ji A. P., Frebel A., Simon J. D., Geha M., 2016b, *ApJ*, **817**, 41
- Ji A. P., Frebel A., Simon J. D., Chiti A., 2016c, *ApJ*, **830**, 93
- Ji A. P., Simon J. D., Frebel A., Venn K. A., Hansen T. T., 2019, *ApJ*, **870**, 83
- Ji A. P., et al., 2020, *ApJ*, **889**, 27
- Kallivayalil N., et al., 2018, *ApJ*, **867**, 19
- Keller S. C., et al., 2014, *Nature*, **506**, 463
- Kelson D. D., 2003, *PASP*, **115**, 688
- Kerr F. J., Lynden-Bell D., 1986, *MNRAS*, **221**, 1023
- Kirby E. N., Simon J. D., Geha M., Guhathakurta P., Frebel A., 2008, *ApJ*, **685**, L43
- Kirby E. N., Cohen J. G., Simon J. D., Guhathakurta P., Thygesen A. O., Duggan G. E., 2017, *ApJ*, **838**, 83
- Koch A., McWilliam A., Grebel E. K., Zucker D. B., Belokurov V., 2008, *ApJL*, **688**, L13
- Koch A., et al., 2009, *ApJ*, **690**, 453
- Koch A., Feltzing S., Adén D., Matteucci F., 2013, *A&A*, **554**, A5
- Lai D. K., Bolte M., Johnson J. A., Lucatello S., Heger A., Woosley S. E., 2008, *ApJ*, **681**, 1524
- Lai D. K., Lee Y. S., Bolte M., Lucatello S., Beers T. C., Johnson J. A., Sivarani T., Rockosi C. M., 2011, *ApJ*, **738**, 51
- Lee Y. S., Beers T. C., Kim Y. K., Placco V., Yoon J., Carollo D., Masseron T., Jung J., 2017, *ApJ*, **836**, 91
- Lee Y. S., Beers T. C., Kim Y. K., 2019, *ApJ*, **885**, 102
- Li H.-N., Aoki W., Honda S., Zhao G., Christlieb N., Suda T., 2015, *Research in Astronomy and Astrophysics*, **15**, 1264
- Luri X., et al., 2018, *A&A*, **616**, A9
- Maeder A., Meynet G., Chiappini C., 2015, *A&A*, **576**, A56
- Mardini M. K., et al., 2019, *ApJ*, **875**, 89
- Mardini M. K., et al., 2020, *ApJ*, **903**, 88
- Mardini M. K., et al., 2022a, *MNRAS*, **517**, 3993
- Mardini M. K., Frebel A., Chiti A., Meiron Y., Brauer K. V., Ou X., 2022b, *ApJ*, **936**, 78
- Mardini M. K., Frebel A., Betre L., Jacobson H., Norris J. E., Christlieb N., 2024, *MNRAS*, **528**, 2912
- Marshall J. L., et al., 2019, *ApJ*, **882**, 177
- McMillan P. J., 2017, *MNRAS*, **465**, 76
- Meynet G., Ekström S., Maeder A., 2006, *A&A*, **447**, 623
- Nagasawa D. Q., et al., 2018, *ApJ*, **852**, 99
- Norris J. E., Christlieb N., Korn A. J., Eriksson K., Bessell M. S., Beers T. C., Wisotzki L., Reimers D., 2007, *ApJ*, **670**, 774
- Norris J. E., Yong D., Gilmore G., Wyse R. F. G., 2010, *ApJ*, **711**, 350
- Orkney M. D. A., et al., 2022, *MNRAS*, **515**, 185
- Placco V. M., et al., 2014a, *ApJ*, **790**, 34
- Placco V. M., Frebel A., Beers T. C., Stancliffe R. J., 2014b, *ApJ*, **797**, 21
- Placco V. M., Frebel A., Lee Y. S., Jacobson H. R., Beers T. C., Pena J. M., Chan C., Heger A., 2015, *ApJ*, **809**, 136
- Placco V. M., Sneden C., Roederer I. U., Lawler J. E., Den Hartog E. A., Hejazi N., Maas Z., Bernath P., 2021, *Research Notes of the American Astronomical Society*, **5**, 92
- Purandardas M., Goswami A., 2021, *ApJ*, **912**, 74
- Roederer I. U., Preston G. W., Thompson I. B., Shtetman S. A., Sneden C., Burley G. S., Kelson D. D., 2014, *AJ*, **147**, 136
- Roederer I. U., et al., 2016, *AJ*, **151**, 82
- Roederer I. U., Hattori K., Valluri M., 2018, *AJ*, **156**, 179
- Ryan S. G., Norris J. E., Beers T. C., 1996, *ApJ*, **471**, 254
- Safarzadeh M., Spergel D. N., 2020, *ApJ*, **893**, 21
- Schlafly E. F., Finkbeiner D. P., 2011, *ApJ*, **737**, 103
- Schönrich R., 2012, *MNRAS*, **427**, 274
- Schönrich R., Binney J., Dehnen W., 2010, *MNRAS*, **403**, 1829
- Sestito F., et al., 2024, *MNRAS*, **528**, 4838
- Simon J. D., 2019, *ARA&A*, **57**, 375
- Simon J. D., Geha M., 2007, *ApJ*, **670**, 313
- Simon J. D., Frebel A., McWilliam A., Kirby E. N., Thompson I. B., 2010, *ApJ*, **716**, 446
- Simon J. D., et al., 2023, *ApJ*, **944**, 43
- Sneden C. A., 1973, PhD thesis, University of Texas, Austin
- Sobeck J. S., et al., 2011, *AJ*, **141**, 175
- Spite M., Spite F., François P., Bonifacio P., Caffau E., Salvadori S., 2018, *A&A*, **617**, A56
- Suda T., et al., 2017, *PASJ*, **69**, 76
- Vargas L. C., Geha M., Kirby E. N., Simon J. D., 2013, *ApJ*, **767**, 134
- Venn K. A., Irwin M., Shetrone M. D., Tout C. A., Hill V., Tolstoy E., 2004, *AJ*, **128**, 1177
- Virtanen P., et al., 2020, *Nature Methods*, **17**, 261
- Waller F., et al., 2022, *arXiv e-prints*, p. [arXiv:2208.07948](https://arxiv.org/abs/2208.07948)
- Wanajo S., Ishimaru Y., 2006, *Nuclear Physics A*, **777**, 676
- Weisz D. R., Dolphin A. E., Skillman E. D., Holtzman J., Gilbert K. M., Dalcanton J. J., Williams B. F., 2014, *ApJ*, **789**, 148
- Wes McKinney 2010, in Stéfan van der Walt Jarrod Millman eds, *Proceedings of the 9th Python in Science Conference*. pp 56 – 61, doi:10.25080/Majora-92bf1922-00a

- Wetzel A. R., Hopkins P. F., Kim J.-h., Faucher-Giguère C.-A., Kereš D., Quataert E., 2016, *ApJ*, **827**, L23
- Wheeler C., Oñorbe J., Bullock J. S., Boylan-Kolchin M., Elbert O. D., Garrison-Kimmel S., Hopkins P. F., Kereš D., 2015, *MNRAS*, **453**, 1305
- Wisotzki L., Koehler T., Grootte D., Reimers D., 1996, *A&AS*, **115**, 227
- Yong D., et al., 2013, *ApJ*, **762**, 26
- Yong D., et al., 2021, *Nature*, **595**, 223
- Yoon J., et al., 2018, *ApJ*, **861**, 146
- Yuan Z., et al., 2020, *ApJ*, **891**, 39
- Zacharias N., Finch C. T., Girard T. M., Henden A., Bartlett J. L., Monet D. G., Zacharias M. I., 2013, *AJ*, **145**, 44

This paper has been typeset from a $\text{\TeX}/\text{\LaTeX}$ file prepared by the author.